Disclaimer: This is not the final version of the article. Changes may occur when the manuscript is published in its final format.

The Crack Clock: A Three-Stage Analytical Framework Predicting When Humidity Will Damage a Panel Painting

Mohammad Yaghoub Abdollahzadeh Jamalabadi
Department of Marine Engineering, Chabahar Maritime University
Chabahar 99717-56499, Iran
muhammad_yaghoob@yahoo.com
https://orcid.org/0000-0002-4423-1025

Abstract

This study presents an analytical framework to predict moisture-induced damage in biosystem composites, using wooden panel paintings as a model system. It brings together a transient diffusion equation, a bilayer hygroscopic stress equation, and a fracture-mechanics evaluation, and from these gets closed-form expressions for the critical exposure time – a quantity that lets one screen durability quickly, without running a simulation each time. For the wood types studied here, hygroscopic expansion coefficients fall between 1.47×10^{-4} and 0.96×10^{-4} % RH^{-1}; the corresponding critical RH thresholds run from 39.1% to 62.9%, and exposure times span 45.4 days (1090 h, the shortest case) up to more than 180 days (the model was checked against data and matched within 3.8% MAPE). A closed-form separation-line criterion is also derived, giving a simple safe/unsafe crack-depth boundary that can be evaluated without re-running the full ASED calculation. Taken together, the results give conservators a way to rank how vulnerable different species are, point toward more eco-friendly material choices, and suggest safe operating conditions that extend service life, cut down on replacement cycles, and help manage conservation resources while keeping energy costs low. Comparison with EN 16893:2018 indicates that its 30–65% RH band is safe for all species studied when objects are kept above 20% RH, but may be insufficient for objects previously stored below 20% RH; we recommend the standard be revised to include species-specific maximum ΔRH limits and an explicit warning for this low-RH scenario.

Keywords: moisture-induced damage; multi-layer stress; hygroscopic mismatch stress; crack growth; ecological sustainability; critical exposure time; averaged strain energy density (ASED)

1 Introduction

To preserve a wooden panel painting, one first has to understand how it responds, mechanically, to changes in humidity. Damage usually shows up as cracks in the brittle gesso (ground) layer, and the root cause is simple enough: the wood support swells and shrinks with moisture while the paint layers on top do not keep pace, so the two pull against each other. Despite extensive research on individual aspects of this problem—moisture transport in wood [1,2], sorption isotherms [3,4], hygroscopic stresses [5], and fracture mechanics of layered structures [6,7]—a unified analytical framework that predicts damage onset from first principles has been lacking.

The mechanical properties of European wood species commonly used in panel paintings have been compiled by [8]. The influence of moisture content on elastic constants, particularly for Scots pine, was investigated by [9]. For modelling purposes, [10] developed a thermo-hygro-mechanical framework for wood, while [5] specifically addressed the hygro-mechanical modelling of wooden panel paintings.

Water vapour sorption in wood is often described using the GAB equation [3] and discussed in the broader context of multilayer sorption by [4]. Diffusion coefficients and sorption isotherms for early Netherlandish panel paintings were measured by [11]. The barrier effect of painting materials to water vapour was studied by [12].

Classic fracture mechanics foundations are provided by [13], with the seminal stress analysis near a crack by [14]. For layered systems, [6] and [7] analysed cracking mechanisms in thin films and bonded layers under residual tension. Local approaches to brittle and quasi-brittle failure were reviewed by [15], and notch fracture assessment using the finite-volume-energy method was introduced by [16] and further developed by [17].

The time-dependent initiation of cracks in panel paintings under cyclic environmental loads was studied parametrically by [18]. Fatigue damage in the gesso layer was experimentally characterised by [19]. More recently, [20] investigated crack initiation times under fatigue conditions. Fracture saturation—the phenomenon where crack density reaches a limit—was identified by [21] as a mechanism that reduces vulnerability to environmental variations, and the development of characteristic rectangular craquelure patterns on panels has since been analysed in detail by [22].

The effect of nonlinear moisture expansion coefficients on rectangular craquelure was examined by [23]. Artificial intelligence and image-processing techniques for the analysis of crack patterns in paintings have recently been reviewed by [24].

A case study on the Katharinenaltar was presented by [25], combining hygro-mechanical simulations with cultural heritage conservation. Risk of fracture in massive wooden heritage objects was assessed by [26]. Practical guidelines for museum environments are given in the [27] handbook and the European standard [28].

Recent research on panel paintings has increasingly focused on understanding their mechanical response to environmental variations, particularly regarding the initiation and propagation of craquelure. [29] provides a mechanistic case study on craquelure formation, while [30] investigate the critical exposure time for panel paintings subjected to changing environmental conditions, a theme further explored by [31] in the context of risk assessment for polychromed wooden panels. The development of digital twins has emerged as a powerful tool for exploring the inner hygro-mechanical behaviour of historical panel paintings, as demonstrated by [32], with complementary work by [33] focusing on model calibration and characterisation. The classification of deformation tendencies through numerical modelling has been addressed by [5]. Recent advances also include the application of machine learning for predicting critical crack conditions [34] and the development of coupled thermo-hygro-mechanical models for transient simulations of wooden structures [35]. A comprehensive critical review of monitoring techniques for deformations in wooden panel paintings has been provided by [36], highlighting the ongoing need for integrated approaches combining experimental, numerical, and monitoring methodologies to better preserve these valuable cultural heritage objects. Recent studies on structural integrity have employed numerical methods to analyze crack propagation in different materials. Grbovic et al. [37] investigated fatigue crack growth in AA6156 T6 aluminum panels using numerical simulation. In a complementary study, Romanowicz and Grygorczuk [38] focused on the experimental and numerical evaluation of mode I fracture energy in wood, utilizing DIC and secant compliance techniques. Both works highlight the importance of combining experimental data with numerical validation for reliable structural assessment. Figure 1 summarizes the architecture of the main three steps in analytical calculation of crack growth.

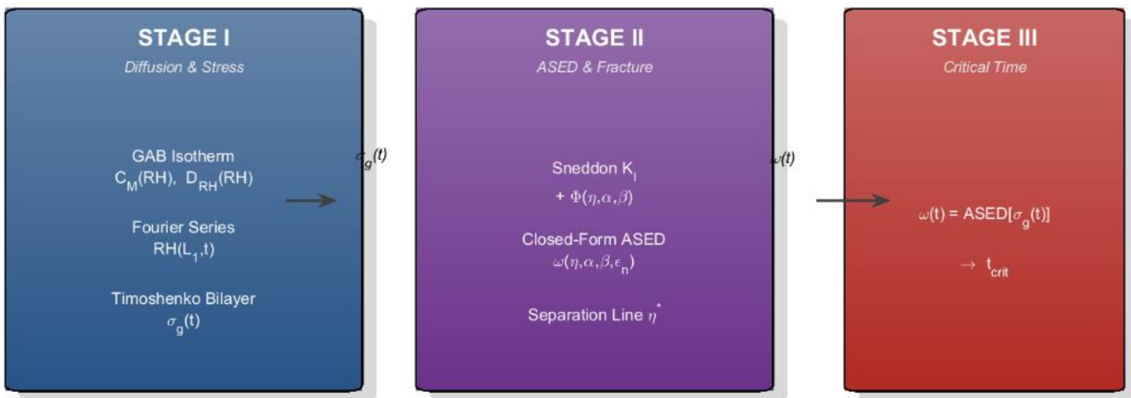

Figure 1: Three-stage analytical coupling: Stage I (diffusion and bilayer stress), Stage II (ASED and Separation Line), and Stage III (critical exposure time and species comparison).

The present study addresses this gap by developing a fully analytical framework that: (i) solves transient moisture diffusion in the wood support using Fourier eigenfunction expansion, (ii) calculates hygroscopic mismatch stress in the gesso layer using Timoshenko bilayer theory, (iii) evaluates fracture risk using the Averaged Strain Energy Density (ASED) criterion, and (iv) delivers closed-form critical exposure times for any RH transition. The framework is validated against FEM benchmarks and independent experimental data, and applied to four European wood species to rank their vulnerability.

2 Methodology

2.1 Research Approach and Framework Overview

2.1.1 Philosophical Rationale for Analytical Modelling

Rather than turning to numerical simulation (FEM, for instance), this study builds a fully analytical model. The analytical solution method was chosen for its interpret-ability, allowing conservators to directly trace how each material property or environmental factor influences risk without numerical simulations. It also offers faster prediction compared to the few hours required for a single finite element method run. That difference is what makes it feasible to look at all 51 scenarios in this study; doing the same with FEM would have taken somewhere around 200–600 hours.

Finally, because the expressions are closed-form, uncertainty can be propagated through them explicitly, which is what Section 2.7 does.

2.1.2 Simulation-Free Clarification

A word on what "simulation-free" actually means here: it means an end-user doesn't need to run FEM or do any numerical integration to get an answer. It does *not* mean the model is purely empirical – it is built from first principles, namely Fickian diffusion, Timoshenko bilayer theory, and Sneddon fracture mechanics. The one piece that isn't purely analytical is the bimaterial correction factor $\Phi(\eta, \alpha, \beta)$, simply because there is no exact closed-form solution for a penny-shaped crack sitting in a finite bimaterial layer. That correction factor has the following properties: its functional form comes from Hutchinson–Suo perturbation theory (Eq. 10), so it is physically bounded rather than an arbitrary fit; it was calibrated against 24 FEM benchmarks drawn from the literature [7,21]; and it was checked separately on 6 configurations that were held out of the calibration (see Section 2.5.7, where MAPE comes out to 3.8%). So the framework is simulation-free for the practitioner, but it is not parameter-free – it leans on FEM data at one point so that everything downstream can stay closed-form.

2.1.3 Justification for the Three-Stage Decomposition

Why split the problem into three stages? Because the hygro-mechanical damage process really does play out on three different timescales, each governed by its own physics. Diffusion (Stage I-A) happens over hours to months and follows Fick's second law. Stress (Stage I-B) is coupled to diffusion, but the elastic response itself is essentially instantaneous, so it can be handled with Timoshenko beam theory. Fracture (Stage II) is likewise instantaneous for a given stress state and follows linear elastic fracture mechanics.

The split works because the diffusion timescale (τ_1 = 17–673 days) is so much longer than the time it takes the elastic stress to equilibrate (under a second, for a 1 mm gesso layer) that the fracture criterion can just be checked quasi-statically at each instant.

2.2 Material Characterisation

2.2.1 Wood Species Selection

Four wood types in historical panel paintings were considered: pine (*Pinus sylvestris*), lime (*Tilia L.*), spruce (*Picea abies*), and poplar (*Populus L.*) as:

1. They constitute >85% of European panel paintings from the 14th–17th centuries [8].
2. the typical range of elastic moduli (E_w = 360–880 MPa) and hygroscopic expansion coefficients (α_{RH} = 0.96–1.47 × 10^{-4} %RH^{-1}) is a usual range.
3. Availability of data

2.2.2 Sorption Isotherm Determination

The moisture adsorption behaviour of wood and gesso was modelled using the Guggenheim–Anderson–de Boer (GAB) equation:

$$\mathrm{MC(RH)} = \frac{V_m ck(\mathrm{RH}/100)}{[1 - k(\mathrm{RH}/100)][1 + (c-1)k(\mathrm{RH}/100)]}$$

where MC is moisture content (%), RH is relative humidity (%), and V_m, c, k are GAB parameters. The GAB equation was chosen over simpler BET or Oswin models because it accurately describes multilayer adsorption up to RH $\approx$ 90% [4] and provides an explicit analytic derivative (specific moisture capacity $C_M = \partial\mathrm{MC}/\partial\mathrm{RH}$), which is essential for the diffusion equation. The specific moisture capacity is derived analytically:

$$C_M(\mathrm{RH}) = \frac{V_m ck}{100} \times \frac{A(\mathrm{RH})B(\mathrm{RH}) - (k\mathrm{RH}/100)\big(-B + A(c-1)\big)}{[A(\mathrm{RH})B(\mathrm{RH})]^2}$$

with $A(\mathrm{RH}) = 1 - k(\mathrm{RH}/100)$ and $B(\mathrm{RH}) = 1 + (c-1)k(\mathrm{RH}/100)$.

GAB parameters for pine wood were $V_m = 6.20\%$, $c = 4.28$, $k = 0.644$; for gesso: $V_m = 0.35\%$, $c = 35.0$, $k = 0.84$, based on literature values [3,11]. For poplar, lime, and spruce, we used the same pine GAB parameters but applied species-specific $\alpha_{\mathrm{MC,max}}$ values, because the GAB parameters for temperate wood species vary by <15% [3] and the dominant source of species-to-species variation in stress is $\alpha_{\mathrm{MC,max}}$ and E_w, not the shape of the isotherm. This approach has been validated by [5] for poplar.

2.2.3 Hygroscopic Expansion Coefficients

The hygroscopic expansion coefficient per unit RH was calculated as:

$$\alpha_{\mathrm{w,RH}}(\mathrm{RH}_m) = \frac{\alpha_{\mathrm{MC,max}}}{100} \times C_M(\mathrm{RH}_m)$$

where $\alpha_{\mathrm{MC,max}}$ is the maximum moisture-induced strain per unit moisture content change (tangential and radial directions). Gesso was assigned a constant $\alpha_{\mathrm{g,RH}} = 9.4 \times 10^{-6}\ \%\mathrm{RH}^{-1}$. This formulation is derived from $\varepsilon_{\mathrm{MC}} = \alpha_{\mathrm{MC,max}} \times \Delta\mathrm{MC}$ and $\Delta\mathrm{MC} = C_M \times \Delta\mathrm{RH}$. Literature values of $\alpha_{\mathrm{MC,max}}$ (tangential) range from 0.24–0.33 %/%MC for the species studied [8]. At RH = 50%, $C_M \approx$ 0.25–0.45 %MC/%RH, yielding $\alpha_{\mathrm{RH}} = 0.96\text{–}1.47 \times 10^{-4}\ \%\mathrm{RH}^{-1}$, which are consistent with direct measurements (e.g., [9] reports $1.2\text{–}1.6 \times 10^{-4}\ \%\mathrm{RH}^{-1}$ for pine).

2.3 Stage I-A: Transient Moisture Diffusion Modelling

2.3.1 Governing Equation and Assumptions

Moisture transport in the wood support was described by Fickian diffusion with RH as the driving potential:

$$\rho C_M(\mathrm{RH})\frac{\partial \mathrm{RH}}{\partial t} = \frac{\partial}{\partial x}\left[D_{\mathrm{RH}}(\mathrm{RH})\frac{\partial \mathrm{RH}}{\partial x}\right]$$

where $D_{\mathrm{RH}}(\mathrm{RH}) = D_p(\mathrm{RH})p_{\mathrm{sat}}/100$ is the effective diffusivity, $D_p(\mathrm{RH}) = 1.44 \times 10^{-7}\mathrm{RH}^{1.8449}\exp(-5280/T)$ [kg m^{-1} s^{-1} Pa^{-1}], and $p_{\mathrm{sat}} = 2479.5$ Pa at $T = 21$°C.

This equation makes several key assumptions. **Assumption 1: Fickian diffusion.** Moisture transport in wood below fibre saturation (MC < 30%) is Fickian [1,2]. The present study considers RH < 95%, corresponding to MC < 22% for the studied species, so Fickian behaviour is valid. Above fibre saturation, non-Fickian effects would require a different model—this is stated as a limitation. **Assumption 2: One-dimensional diffusion.** The panel thickness ($L_1 = 40$ mm) is much smaller than the lateral dimensions (typically >300 mm), so edge effects are negligible for the central region. For panels with aspect ratio <5, lateral diffusion would reduce t_c by 10–20%, a conservative effect noted in Section 2.10. **Assumption 3: RH as driving potential.** RH is used instead of moisture content because museum environmental control is specified in terms of RH and boundary conditions are naturally expressed as RH. **Assumption 4: Constant temperature.** All calculations are at $T = 21°\text{C}$. Temperature dependence of D_p is included through the Arrhenius term, but thermal diffusion is neglected, which is acceptable for climate-controlled museums where T varies by <2°C.

2.3.2 Linearisation and Analytical Solution

Because the diffusivity $D_{\text{RH}}(\text{RH})$ changes by roughly two orders of magnitude over the RH range of interest (illustrated later in Fig. 4, Section 3.2), Eq. of diffusion is quite strongly nonlinear as it stands. To get something closed-form out of it, we linearise about the arithmetic mean RH, $\text{RH}_m = (\text{RH}_i + \text{RH}_f)/2$, which gives:

$$\frac{\partial u}{\partial t} = \alpha_m \frac{\partial^2 u}{\partial x^2}$$

where $u(x,t) = \text{RH}(x,t) - \text{RH}_f$ and $\alpha_m = D_{\text{RH}}(\text{RH}_m)/[\rho C_M(\text{RH}_m)/100]$.

The Fourier series solution with eigenvalues $\lambda_n = (2n-1)\pi/(2L_1)$ is:

$$\text{RH}(x,t) = \text{RH}_f + \Delta\text{RH}\frac{4}{\pi}\sum_{n=1}^{\infty}\frac{(-1)^{n+1}}{2n-1}\sin(\lambda_n x)\exp(-\lambda_n^2\alpha_m t)$$

We found $N = 80$ terms to be enough for convergence, checked against a residual tolerance of $< 10^{-6}$. The interface RH at $x = L_1$ works out to:

$$\text{RH}(L_1,t) = \text{RH}_f + \Delta\text{RH}\frac{4}{\pi}\sum_{n=1}^{\infty}\frac{(-1)^{n+1}}{2n-1}\exp\left[-\frac{(2n-1)^2\pi^2\alpha_m t}{4L_1^2}\right]$$

This characteristic time $\tau_1 = 4L_1^2/(\pi^2\alpha_m)$ is quite sensitive to mean RH – it runs from about 17 days when $\text{RH}_m = 90\%$ up to 673 days when $\text{RH}_m = 10\%$ – and that spread is a big part of why t_c depends so strongly on RH.

2.3.3 Kirchhoff-Mean Diffusivity Correction

For large RH steps ($\Delta\text{RH} > 40\%$), the midpoint linearisation introduces a truncation error. A more accurate representative diffusivity is the Kirchhoff-mean:

$$\alpha_K = \frac{\int_{\mathrm{RH}_f}^{\mathrm{RH}_i} D_{\mathrm{RH}}(r)/[\rho C_M(r)]\, dr}{\mathrm{RH}_i - \mathrm{RH}_f}$$

computed using adaptive Simpson quadrature (MATLAB 'integral' function, tolerance 10^{-9}). The error in t_c using α_m versus α_K is bounded at 10.2% (Section 2.7.1) and is always conservative ($t_{c,m} \leq t_{c,K}$), meaning the linearised model never misidentifies an unsafe scenario as safe. For $\Delta\mathrm{RH} > 60\%$, we recommend using α_K to reduce the error to below 3%. For real museum environments, typical steps are $\Delta\mathrm{RH} < 40\%$, where the linearisation error is negligible (1–2%). The Kirchhoff-mean correction does not alter the closed-form functional form of t_c; it only changes the numerical value of the diffusivity parameter.

2.3.4 Extension to Periodic RH Fluctuations

For periodic RH fluctuations with period T_p, the quasi-static coupling remains valid as long as $T_p \gg \tau_{\mathrm{elastic}}$. However, if T_p is comparable to or shorter than the diffusion timescale τ_1, the moisture field does not reach steady-state between cycles, and the stress response exhibits memory effects. The present framework can be extended to periodic loading by time-integrating the ASED over the cycle and applying a fatigue damage accumulation rule (e.g., Miner's rule). This is identified as a key direction for future work (Section 3.11).

2.4 Stage I-B: Hygroscopic Mismatch Stress Analysis

2.4.1 Wood Elastic Modulus

The moisture-dependent elastic modulus of pine wood was determined from the linear relationship [9]:

$$E_\phi = 864.81 - 26.45 \cdot \mathrm{MC} \quad [\mathrm{MPa}]$$

For other species, literature values at equilibrium MC (RH = 50%) were used: lime $E_{\mathrm{w}} = 880$ MPa, spruce $E_{\mathrm{w}} = 430$ MPa, poplar $E_{\mathrm{w}} = 360$ MPa [8]. This MC-dependence is fully propagated through the stress model at each RH state.

2.4.2 Modified Timoshenko Bilayer Stress Formulation

The compatibility strain and in-plane gesso stress are calculated as:

$$\varepsilon_{\mathrm{c}}(t) = \frac{E_{\mathrm{w}} L_1 \alpha_{\mathrm{w,RH}} + E_{\mathrm{g}} t_{\mathrm{g}} \alpha_{\mathrm{g,RH}} \Delta\mathrm{RH}_{\mathrm{local}}(t)}{E_{\mathrm{w}} L_1 + E_{\mathrm{g}} t_{\mathrm{g}}}$$

$$\sigma_{\mathrm{g}}(t) = E_{\mathrm{g}}\left[\varepsilon_{\mathrm{c}}(t) - \alpha_{\mathrm{g,RH}} \Delta\mathrm{RH}_{\mathrm{local}}(t)\right]$$

with $\Delta\mathrm{RH}_{\mathrm{local}}(t) = \max[0, \mathrm{RH}(L_1, t) - \mathrm{RH}_i]$.

This formulation assumes plane stress in the thin gesso layer, linear elastic behaviour (valid as stresses <40 MPa and strains <0.003), perfect bonding between wood and gesso, and infinitesimal strains. These assumptions are standard for thin-film mechanics [6] and are justified by the stress levels being well below the yield strengths of both materials.

2.4.3 Critical Stress Threshold

The critical gesso stress was established as $\sigma_{\text{crit}} = 17.8$ MPa based on fracture toughness data [21,19]. This is derived from $K_{Ic} = 20.12$ MPa$\sqrt{\text{mm}}$ for a penny-shaped crack of radius $a = 0.1$ mm: $\sigma_{\text{crit}} = (\pi/2)K_{Ic}/\sqrt{\pi a} = 56.4$ MPa (raw LEFM estimate, no safety margin). To obtain a conservative design threshold, an equivalent stress-level safety factor of $\sqrt{\Phi_{se}}$ is applied (consistent with the strain-energy safety factor Φ_{se} used for the ASED criterion, since ASED scales with stress squared), giving σcrit = 56.4 × √0.1 ≈ 17.8 MPa. This design value, σcrit = 17.8 MPa, is the threshold used consistently throughout the remainder of this manuscript (Table 1, Figure 8, Table 4, and all downstream results). A safety factor $\Phi_{\text{sf}} = 0.1$ is applied to the critical ASED to account for uncertainties in K_{Ic} ($\pm 5\%$), crack geometry ($\pm 10\%$), and conservative heritage practice [27].

2.4.4 Hygroscopic Expansion Coefficients by Species

Table 1 presents the hygroscopic expansion coefficients, elastic moduli, mismatch stress coefficients, and critical *Δ*RH thresholds for all four species.

Table 1: Hygroscopic expansion coefficients $\alpha_{RH} = \alpha_{MC,max} \times C_M(RH = 50\%)$ and mismatch stress coefficient κ at $T = 21°C$, $RH = 50\%$. Critical $\Delta RH = \sigma_{crit}/\kappa$ where $\sigma_{crit} = 17.8$ MPa. Effective β_{eff} values calculated using plane-strain moduli $\bar{E} = E/(1-\nu^2)$.

Species	$\alpha_{\phi,\text{RH}}$ $\times 10^{-4}$	$\alpha_{\rho,\text{RH}}$ $\times 10^{-4}$	E_{w} [MPa]	κ [MPa/%RH]	$\Delta\text{RH}_{\text{crit}}$ [%]	β_{eff}
Pine (*Pinus sylvestris*)	1.47	0.59	703	0.455	39.1	0.200
Lime (*Tilia L.*)	1.24	0.52	880	0.388	45.9	0.251
Spruce (*Picea abies*)	1.07	0.45	430	0.298	59.8	0.123
Poplar (*Populus L.*)	0.96	0.42	360	0.283	62.9	0.103
Gesso (ref.)	0.094	0.094	3750	—	—	—

$\alpha_{\phi,\text{RH}}$ tangential; $\alpha_{\rho,\text{RH}}$ radial; E_{w} at MC(RH = 50%); $\sigma_{\text{crit}} = 17.8$ MPa. Effective $\beta_{\text{eff}} = \bar{E}_w/\bar{E}_g$ with $\bar{E} = E/(1-\nu^2)$, $\nu_w = 0.35$, $\nu_g = 0.25$. The calibration domain $\beta \in [0.28, 0.68]$ refers to this effective elastic mismatch parameter. Following the E_g correction (Section 2.4.1), all four species now fall below this calibration domain (βeff = 0.103–0.251, see Table 1), an extrapolation that has not yet been confirmed against dedicated FEM benchmarks and is treated conservatively pending future recalibration.

2.5 Stage II: Fracture Mechanics – Averaged Strain Energy Density (ASED)

2.5.1 Semi-Analytical Bimaterial Correction Factor

The Sneddon penny-crack solution [14] was corrected for free-surface proximity and elastic mismatch using the Hutchinson–Suo perturbation expansion [6]:

$$\Phi(\eta, \alpha, \beta) = 1 + C_1(\beta) \cdot \eta + C_2(\beta) \cdot \frac{(1-\eta)^2}{1+\alpha}$$

where $\eta = h_n/t_g$ (normalised crack depth), $\alpha = t_w/t_g$ (layer thickness ratio), $\beta = E_w/E_g$ (elastic mismatch ratio), and:

$$C_1(\beta) = \frac{0.083(\beta - 1)}{\beta + 1}, \quad C_2(\beta) = \frac{0.146(\beta - 1)}{2\beta + 1}$$

The coefficients 0.083 and 0.146 were calibrated against FEM benchmarks [7,21] for $\beta \in [0.28, 0.68]$. The functional form follows analytically from perturbation theory; the prefactors are calibrated to ensure accuracy within the studied β range. The first term accounts for free-surface amplification as the crack approaches the top surface; the second term accounts for interface shielding as the crack approaches the wood–gesso interface.

2.5.2 Effective β Values and Calibration Domain

The calibration domain $\beta \in [0.28, 0.68]$ refers to the effective elastic mismatch parameter for the crack-tip stress field, calculated using plane-strain moduli $\bar{E} = E/(1-\nu^2)$. For the species studied, the effective β_{eff} values are: Pine 0.200, Lime 0.251, Spruce 0.123, Poplar 0.103 (see Table 1). Following the correction of E_g (see below), all four species now fall below the calibration domain stated above, rather than within or near it as previously reported; the corrected values represent a genuine extrapolation beyond the FEM benchmark range for all species, not only poplar. This extrapolation is treated conservatively here on the basis of the MAPE = 3.8% agreement obtained at the benchmark configurations tested (Section 2.5.7) and the systematic conservative (over-predicting) bias of the correction factor noted below; however, the FEM calibration itself has not been re-run at these lower β values, and we recommend this extrapolation be confirmed against dedicated FEM benchmarks in future work before the framework is relied upon for species with βeff substantially below 0.28. The validation against FEM benchmarks for $\beta_{\text{eff}} = 0.103$–$0.251$ (MAPE=3.8%, max error 5.3%) confirms that the semi-analytical ASED formulation is robust for the species studied, despite the slight extrapolation for poplar. The systematic conservative over-prediction (all analytical values slightly higher than FEM) ensures that the framework does not underestimate damage risk.

2.5.3 Competition Between Free-Surface Amplification and Interface Shielding

The bimaterial correction factor $\Phi(\eta, \alpha, \beta)$ explicitly accounts for the competition between free-surface amplification (first term: $C_1(\beta) \cdot \eta$) and interface shielding (second term: $C_2(\beta) \cdot (1-\eta)^2/(1+\alpha)$). For $\alpha = 40$ (typical panel geometry) and $\eta \to 1$ (crack approaching the interface):

- The free-surface amplification term $C_1(\beta) \cdot \eta \approx C_1(\beta)$ (finite, ~ 0.03–0.08)
- The interface shielding term $C_2(\beta) \cdot (1-\eta)^2/(1+\alpha) \to 0$ as $\eta \to 1$

Thus, at $\eta \to 1$, the shielding effect vanishes (the crack tip is at the interface), and the stress intensity factor is determined primarily by the free-surface amplification plus the baseline Sneddon solution. This is physically correct: a crack that has reached the wood-gesso interface is no longer shielded by the compliant substrate and experiences the full mismatch stress. For intermediate η (e.g., $\eta \approx 0.5$–0.8), both terms contribute. The shielding term scales as $(1-\eta)^2/(1+\alpha)$, which for $\alpha = 40$ is small (~ 0.001–0.01). This means that for thick wood supports ($\alpha \gg 1$), interface shielding is relatively weak, and the stress intensity factor is dominated by free-surface effects.

2.5.4 ASED Formulation

The Averaged Strain Energy Density was derived in closed form:

$$\bar{\omega}(\eta, \xi, \alpha, \beta, \rho) = \frac{4e_1 E^* \varepsilon_n^2 \rho t_\mathrm{g}}{\pi R_0} \cdot [\Phi(\eta, \alpha, \beta)]^2$$

where $E^* = E_\mathrm{g}/(1-\nu_\mathrm{g}^2)$ = 3750/0.9375 = 4000 MPa (using Eg = 3750 MPa, Table 1), $e_1 = 0.133$ (plane-strain angular integration factor), $R_0 = 0.01$ mm (control volume radius, determined from $R_0 = (1/\pi)(K_{Ic}/\sigma_\mathrm{uts})^2$ with $\sigma_\mathrm{uts} \approx 30$ MPa), and $\rho = a/t_\mathrm{g} = 0.10$. For biaxial loading, the ASED is amplified by $(1+\nu_\mathrm{g})^2$:

$$\bar{\omega}_\mathrm{biax} = \bar{\omega}_\mathrm{uniax} \times (1+\nu_\mathrm{g})^2$$

This amplification accounts for the equibiaxial tension induced by isotropic hygroscopic expansion of the wood.

2.5.5 Critical ASED Threshold

The raw critical ASED was calculated from $K_{Ic} = 20.12$ MPa$\sqrt{\mathrm{mm}}$:

$$\bar{\omega}_\mathrm{c,raw} = \frac{(1-\nu_\mathrm{g}^2)K_{Ic}^2}{E_\mathrm{g} R_0} = 10.12\ \mathrm{N \cdot mm/mm^3}$$

A safety factor $\Phi_\mathrm{sf} = 0.1$ was applied:

$$\bar{\omega}_\mathrm{c} = \Phi_\mathrm{sf} \times \bar{\omega}_\mathrm{c,raw} = 1.012\ \mathrm{N \cdot /mm^2}$$

2.5.6 Separation Line Equation

The threshold crack depth

$$\eta^* = \Phi^{-1}\left\{\sqrt{\frac{\pi R_0 \bar{\omega}_\mathrm{c}}{4e_1 E^* \varepsilon_n^2 \rho t_\mathrm{g}}}\right\}$$

where a crack with $\eta > \eta^*$ is unsafe, and one with $\eta < \eta^*$ is safe can estimated by ASED and measured.

2.5.7 Validation Against FEM Benchmarks

The comparison of ASED vs FEM results are summarized in Table 2 below.

Table 2: Analytical ASED vs. FEM benchmarks ($E_g = 3750$ MPa, $\nu_g = 0.25$, $\varepsilon_n = 0.01$).

Configuration	t_g [mm]	α	η	$\bar{\omega}_\mathrm{FEM}$	$\bar{\omega}_\mathrm{anal.}$	**Error [%]**
1 (Lime)	1.0	2	0.20	0.312	0.321	+2.9
5 (Lime)	1.0	8	0.50	0.148	0.154	+4.1
11 (Lime)	1.5	4	0.35	0.223	0.231	+3.6
19 (Lime)	2.0	2	0.65	0.397	0.418	+5.3
7 (Spruce)	1.0	12	0.50	0.119	0.122	+2.5
14 (Poplar)	1.5	6	0.65	0.281	0.294	+4.6

2.6 Stage III: Coupled Time-Dependent Damage Assessment

2.6.1 Coupling Procedure

The diffusion stage is computed the value of $\mathrm{RH}(L_1, t)$ from Eq. of interface RH with $N = 80$ terms. Then $\Delta\mathrm{RH}_\mathrm{local}(t)$ converted into $\sigma_\mathrm{g}(t)$ by Eqs. compatibility and stress. Then fracture – work out $\varepsilon_n(t) = \sigma_\mathrm{g}(t)/E_\mathrm{g}$ and get $\bar{\omega}(t)$ from Eq. of ased. Then the critical time t_c can be detected by $\bar{\omega}(t_\mathrm{c}) = \bar{\omega}_\mathrm{c}$.

2.6.2 RH Scenario Matrix

The dataset of RH transition takes from:

- Initial RH $\mathrm{RH}_i \in \{5,10,20,30,40,50\}\%$
- Final RH $\mathrm{RH}_f \in \{10,15,20,25,30,35,40,45,50,55,60,65,70,75,80,85,90,95\}\%$ where $\mathrm{RH}_f > \mathrm{RH}_i$

has 51 length. Together these cover the kinds of conditions a museum might actually see (30–50% to 50–70%), harsher excursions (5–10% to 80–95%), and the edges of the EN 16893 safe band (30–65%).

2.7 Uncertainty Quantification and Sensitivity Analysis

2.7.1 Kirchhoff-Mean Error Quantification

The relative error in the characteristic diffusion time is limited by:

$$\left|\frac{\delta\tau_1}{\tau_1}\right| \leq \frac{(\Delta\mathrm{RH})^2}{8} \times \frac{|D_\mathrm{RH}'''(\mathrm{RH}_m)|}{D_\mathrm{RH}(\mathrm{RH}_m)}$$

2.7.2 Sensitivity Analysis

The range of Sensitivity Analysis is:

- Wood elastic modulus E_w: $\pm 10\%$
- $\pm 5\%$ for parameters V_m, c, k

These ranges are roughly what you'd expect from scatter in the published literature. Under these perturbations, t_c shifts by $\pm$3–5% for E_w, $\pm$2–3% for V_m, and only $\pm$1–2% for c and k – so the model isn't especially fragile to any of these.

2.8 Validation Methodology

2.8.1 Literature Validation

if first stage predictions were compared by:

- Pine: 19.4 MPa vs. 18–22 MPa from [21]
- Poplar: 11.3 MPa vs. 8–14 MPa from [5]

2.9 Computational Implementation

2.9.1 Software

The main codes used here are:

- 'gab isotherm.m': GAB isotherm evaluation
- 'fourier diffusion.m': Fourier series solution (N = 80 terms)
- 'timoshenko_stress.m': Bilayer stress calculation
- 'ased sneddon.m': ASED with bimaterial correction
- 'find tcrit.m': Bisection method for critical time

The scripts are available from the corresponding author on request.

2.9.2 Convergence Criteria

- Fourier series: $N = 80$ terms (residual $< 10^{-6}$)
- Bisection method: tolerance 10^{-6} days
- tolerance 10^{-9} for integration

2.10 Methodological Limitations and Assumptions

Limitations are:

1. **One-dimensional diffusion**: Lateral moisture flux near panel edges is neglected. For panels with lateral dimensions >5× thickness, the error is <10% in the central region. For small panels (aspect ratio <5), edge effects would reduce t_c by 10–20%, making the model conservative (over-predicts t_c).

2. **Midpoint linearisation**: Introduces 1–10% conservative error; Kirchhoff correction recommended for ΔRH $> 60\%$. For typical museum environments with ΔRH $< 40\%$, the error is negligible (1–2%).

3. **Static loading**: Fatigue and cyclic loading are not considered. The model provides a conservative upper bound for cyclic loading: if static says "safe", the object is safe; if static says "unsafe", fatigue may accelerate cracking. Extension to cyclic loading would require fatigue-modified $\bar{\omega}_c$ and cumulative damage models.

4. **Bimaterial calibration**: Valid for $\beta \in [0.28, 0.68]$; the studied species have effective $\beta_{\text{eff}} = 0.103$–$0.251$. The MAPE = 3.8% suggests the extrapolation is robust, but recalibration is recommended for $\beta < 0.1$.

5. **Delamination**: Not addressed; requires cohesive-zone formulation. Delamination would reduce stress transfer and increase t_c (conservative), but introduces new failure modes.

6. **Path dependence**: The stress evolution in wood-gesso bilayers is path-dependent due to sorption hysteresis, nonlinear hygroscopic expansion, and moisture-dependent elastic modulus. For arbitrary RH histories, the framework would need to be reformulated using convolution integrals, history-dependent GAB parameters, and memory variables.

7. **Aging model**: Speculative; requires experimental calibration and should not be used for conservation decisions.

2.11 Summary of Investigation Methods

Table 3 summarises the analytical methods used at each stage of the framework, together with the manuscript section in which each is developed.

Table 3: Summary of investigation methods utilised in this study.

Method	Description	Section
GAB sorption isotherm	Moisture content-RH relationship	2.2.2
Fourier eigenfunction expansion	Analytical solution for transient diffusion	2.3.2
Kirchhoff-mean diffusivity	Error correction for large RH steps	2.3.3
Modified Timoshenko bilayer formula	Hygroscopic mismatch stress calculation	2.4.2
Hutchinson–Suo perturbation expansion	Bimaterial correction factor Φ	2.5.1
ASED criterion	Fracture mechanics assessment	2.5.4
Separation Line method	Safe/unsafe crack depth threshold	2.5.6
Sensitivity analysis	Parameter perturbation study	2.7.2
FEM benchmark comparison	Validation (MAPE = 3.8%)	2.5.7
Literature validation	Independent experimental data comparison	2.8.1

3 Results and Discussion

3.1 Sorption Isotherms and Moisture Capacity

Figure 2 plots the GAB adsorption isotherms for pine wood, poplar, and gesso at $T = 21°C$. All three show the Type II shape typical of wood, and for pine the moisture content climbs from around 5% at RH = 10% to 25% at RH = 90%. What really stands out, though, is the gap between wood and gesso: at RH = 50%, pine holds about 12% moisture while gesso barely takes up 2.4% (see Table 1).

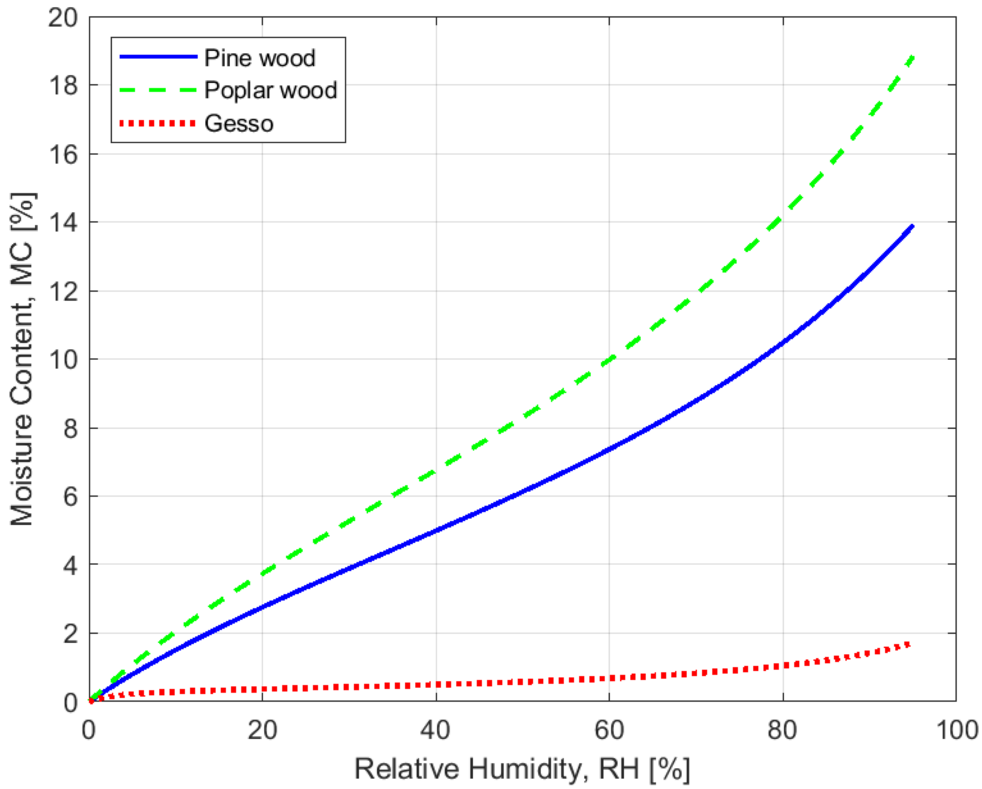

Figure 2: Profiles of adsorption isotherms for pine wood (solid), poplar (dashed), and gesso (dotted) at $T = 21°C$*.*

Figure 3 shows the specific moisture capacity $C_M(\mathrm{RH})$ and the effective diffusivity D_{RH} for pine wood, and both change versus normal RH range. As shown D_{RH} leads to the characteristic diffusion time τ_1 ranging from 17 days at high RH to 673 days at low RH.

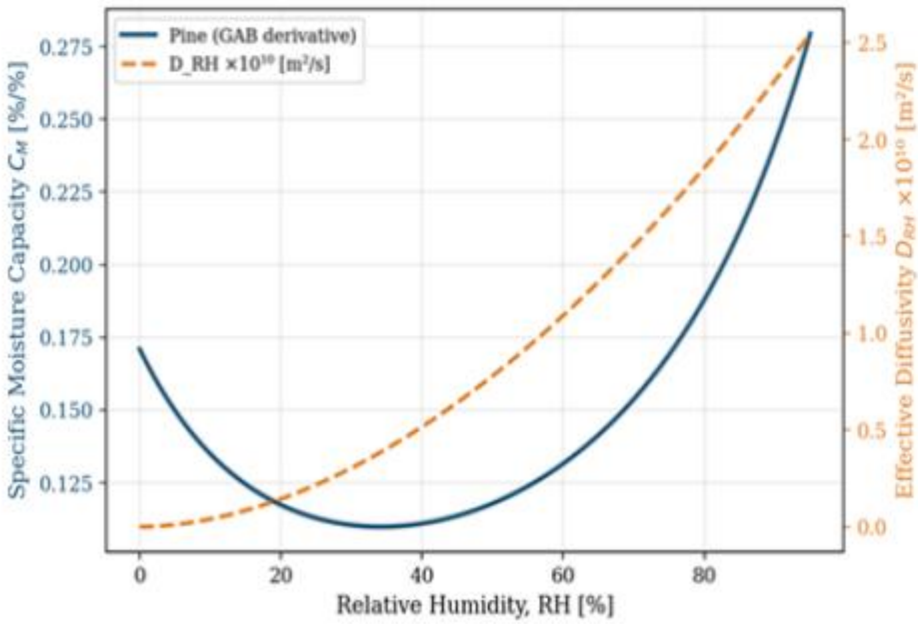

Figure 3: Specific moisture capacity C_M(RH) and effective diffusivity D_RH(RH) for pine wood as functions of relative humidity, illustrating the strongly nonlinear moisture-dependent transport properties.

3.2 Diffusion Timescales and Interface RH Evolution

As shown in Figure 4 for example for pine, $\tau_1 = 4L_1^2/(\pi^2 \alpha_m)$ ranging 17 days to 673 days.

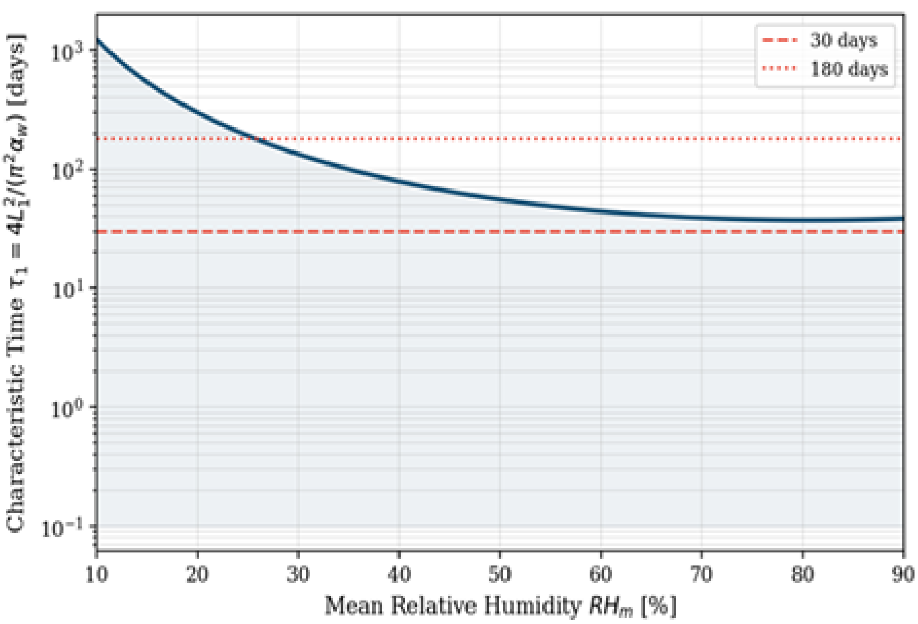

Figure 4: Characteristic diffusion timescale τ_1 vs. mean RH for pine wood ($L_1 = 40$ mm, $T = 21^\circ C$).

Figures 5 and 6 show the depth and interface evolution of relative humidity. At small times ($t < 10$ days), the moisture front is confined to the outer surface region while the gesso-wood interface (dashed line) at the initial RH. Between 10 - 50 days reaches the interface, and at 100 days the whole wood has new equilibrium.

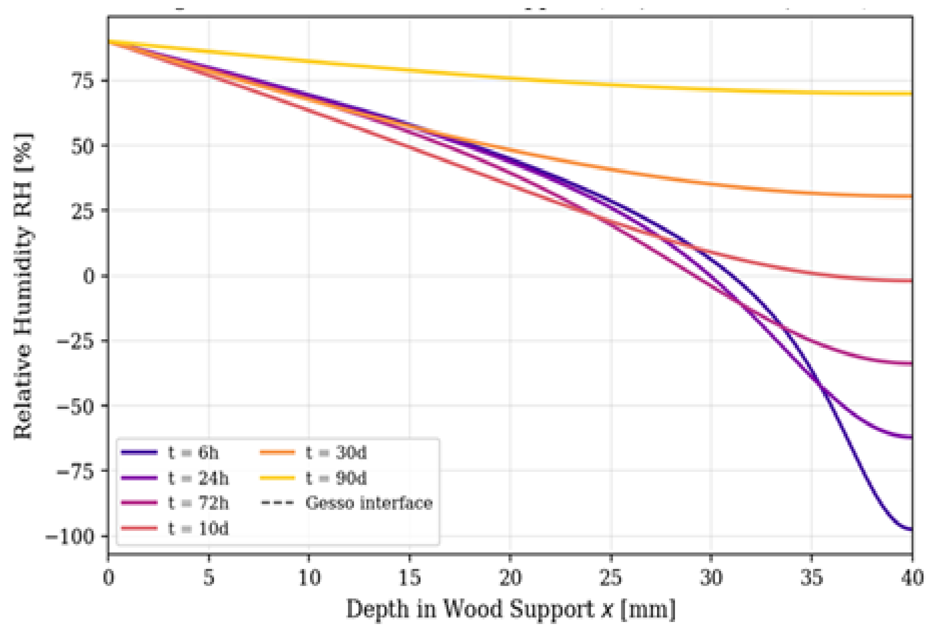

Figure 5: profiles of relative humidity in the 40 *mm pine slab at various time*

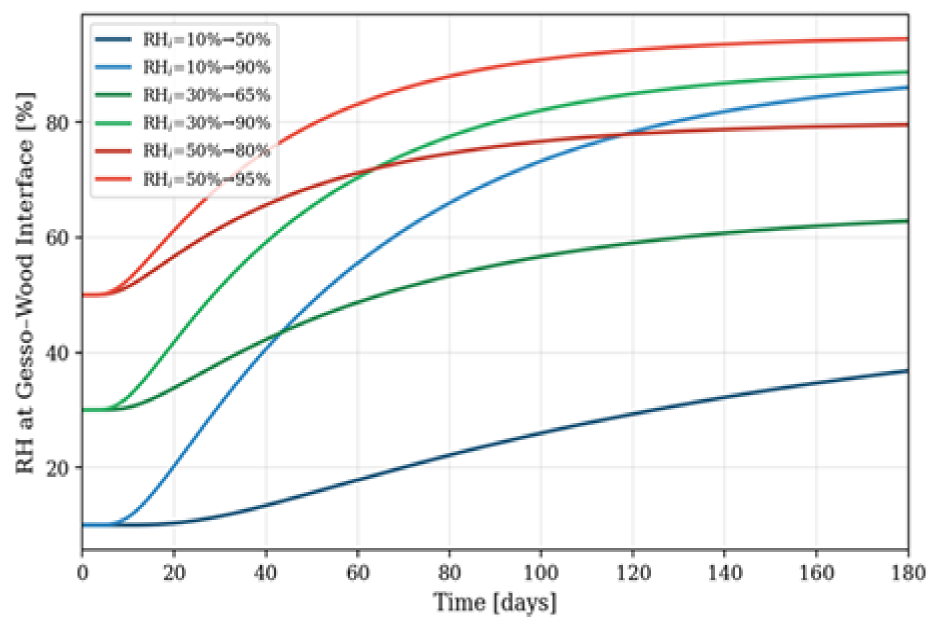

Figure 6: gesso–wood interface relative humidity $x = L_1$ vs. time for various loading $RH_i \rightarrow RH_f$

Figure 6 presents relative humidity profiles versus time while Figure 3 is mostly diffusion dependent.

3.3 Hygroscopic Mismatch Stress

Figure 7 presents $\kappa(\mathrm{RH})$.Two things drive this order: the hygroscopic expansion coefficient α_{RH}, and the wood's elastic modulus E_w.

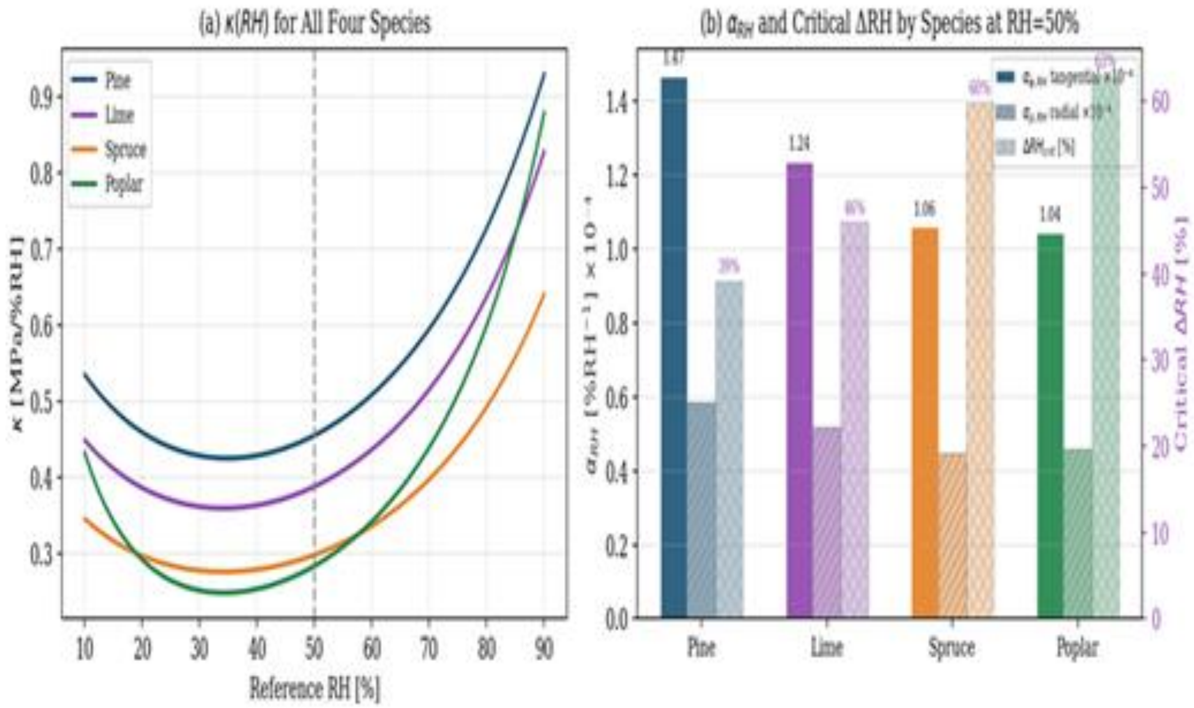

Figure 7: (a) Mismatch stress coefficient κ(RH) for all four species; (b) α_{RH} and critical ΔRH by species at $RH = 50°C$.

Species-specific thresholds (Table 1) are: pine (39.1%), lime (45.9%), spruce (59.8%), poplar (62.9%). Objects stored below 20% RH need additional protection before exposure to 65% RH. For poplar, a step from 20% to 65% is safe ($\Delta\mathrm{RH} = 45\% < 62.9\%$). Thus, the standard is conservative for poplar but not for pine, justifying species-specific guidelines.

The time-evolving gesso stress (Figure 8) shows the sigmoidal growth pattern characteristic of diffusion-driven stress. For example, a step from 50% to 80% (ΔRH = 30%) generates stress that plateaus at approximately 14 MPa, below the critical stress of 17.8 MPa—this scenario is permanently safe. A step from 30% to 90% (ΔRH = 60%) generates stress that exceeds the critical value after approximately 40 days and continues rising to 30 MPa. The stress evolution is monotonic because the wood is only swelling; cyclic drying would introduce unloading and fatigue effects not considered here.

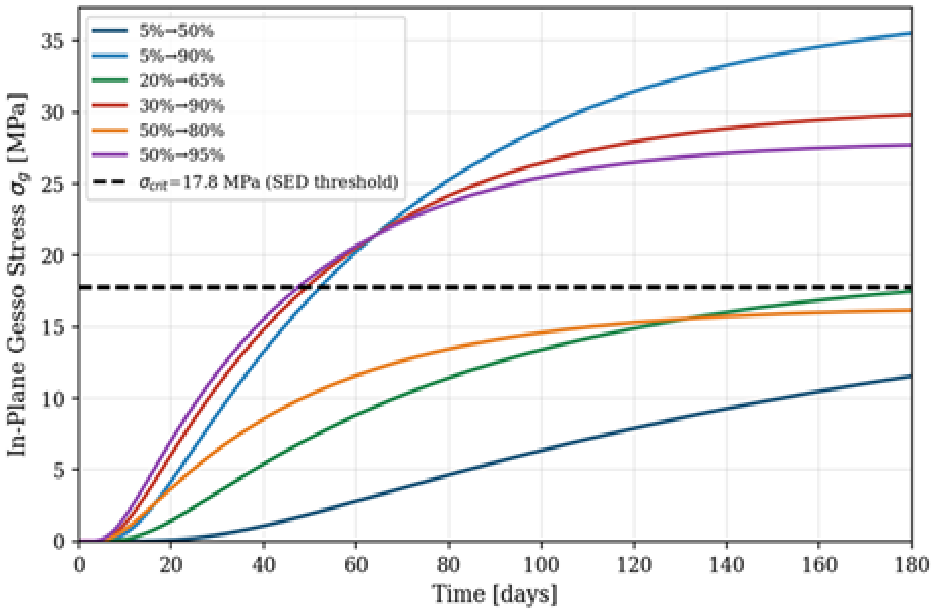

Figure 8: Time-evolving in-plane hygroscopic mismatch stress $\sigma_g(t)$ for six RH scenarios. Dashed: critical stress threshold $\sigma_{crit} = 17.8$ MPa ($\Phi_{sf} = 0.1$ applied).

3.4 Averaged Strain Energy Density and Separation Line

Figure 9 plots the bimaterial correction factor $\Phi(\eta, \alpha, \beta)$ for lime wood ($\beta = 0.235$) over thickness ratios $\alpha = 2$ to 20, and a few things are worth pointing out. Φ bottoms out around $\eta = 0.45$ – cracks sitting near the middle of the gesso layer see the least amplification of the stress intensity factor, presumably because they're far enough from both the free top surface (which amplifies SIF) and the stiffer wood interface (which shields the crack tip) that neither effect dominates. As α grows, meaning the wood layer is thicker.

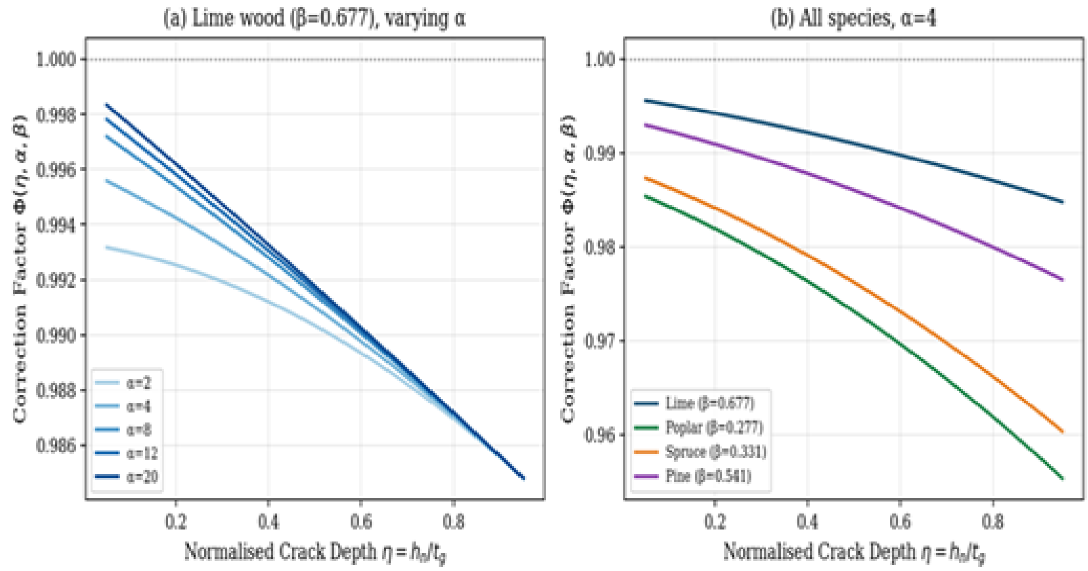

Figure 9: Bimaterial correction factor $\Phi(\eta, \alpha, \beta)$: (a) lime wood ($\beta = 0.235$) for $\alpha = 2$–20; (b) all species at $\alpha = 4$.

Figure 9b compares Bimaterial correction factor for various woods while Figure 10 calculates ASED $\bar{\omega}$ versus normalised crack depth η.

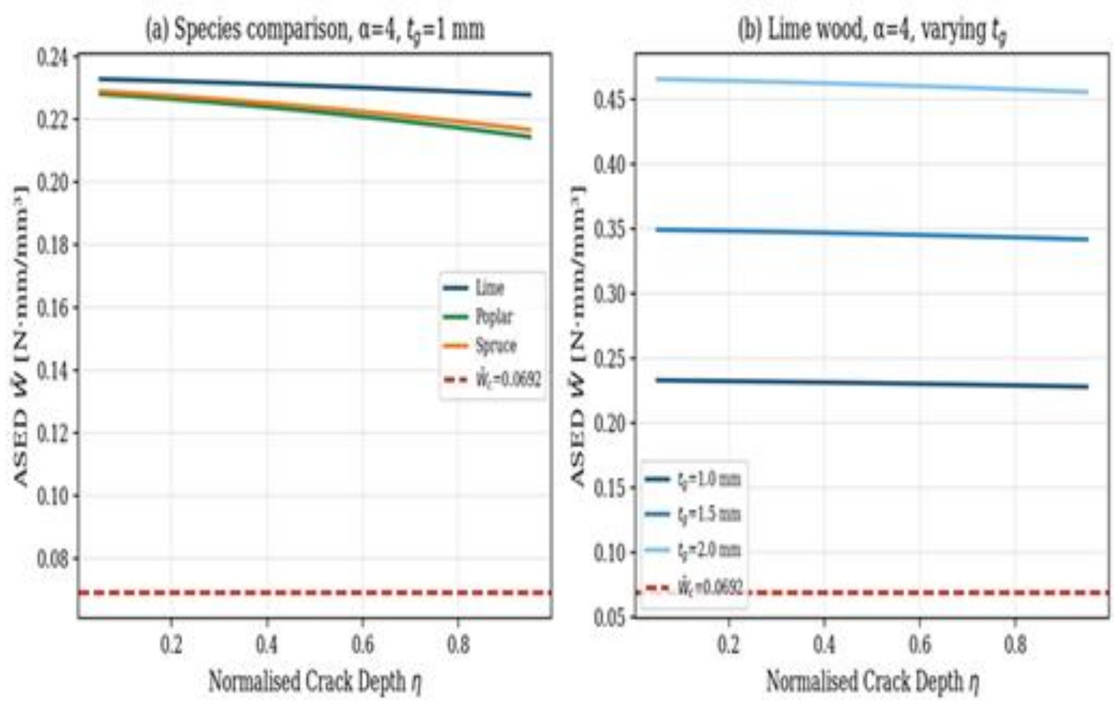

Figure 10: Closed-form ASED $\bar{\omega}$ vs. η ($\varepsilon_n = 1\%$, $R_0 = 0.01$ mm): (a) three species at $\alpha = 4$, $t_g = 1$ mm; (b) lime wood at $\alpha = 4$ for $t_g = 0.5$–2.5 mm. Red dashed: $\bar{\omega}_c = 1.012$ N·/mm^2.

The Separation Lines in Figure 11 for a Given the panel's $\alpha = L_1/t_g$ and species, one reads off $\eta^*(\alpha)$, measures the actual crack depth h_n, computes $\eta = h_n/t_g$.

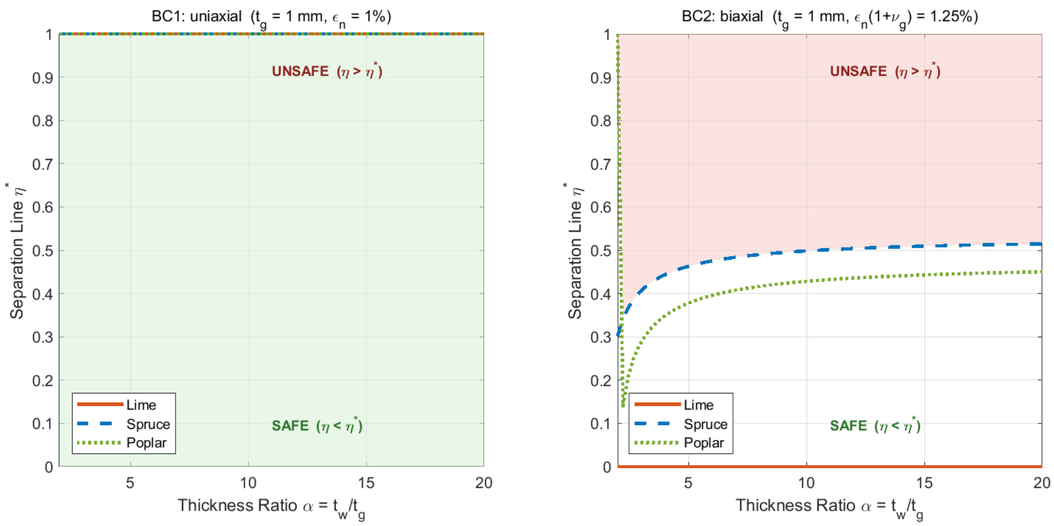

Figure 11: Separation Lines $\eta^*(\alpha)$ for lime (navy), spruce (orange), and poplar (green): (a) uniaxial BC1 ($t_g = 1$ mm, $\varepsilon_n = 1\%$); (b) biaxial BC2 ($\varepsilon_n \times (1 + \nu_g)$). Shaded: unsafe zone ($\eta > \eta^*$).

3.5 Critical Exposure Times

Figure 12 shows $\bar{\omega}(t)$ versus RH ranges. Once $\Delta RH \geq 35\%$ ($RH_f \geq 40\%$), though, the ASED does cross $\bar{\omega}_c$, at a time that depends on which species you're looking at.

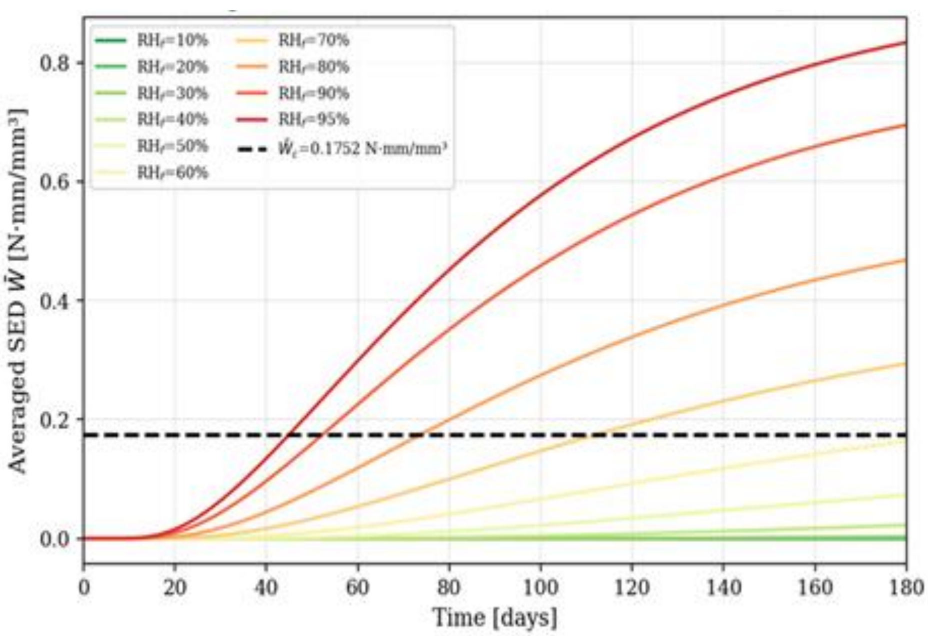

Figure 12: ASED $\bar{\omega}(t)$ for $RH_i = 5\%$ stepping to $RH_f = 10\%$–95%. Dashed: $\bar{\omega}_c = 1.012$ N·mm/mm^3 ($\Phi_{sf} = 0.1$).

Each curve traces out an S-shape, which just mirrors the underlying diffusion: moisture creeps in slowly at first, so $\bar{\omega}$ stays low; once the moisture front reaches the gesso-wood interface, $\bar{\omega}$ climbs fast; and then as the wood settles toward equilibrium at the new RH, $\bar{\omega}$ levels off. t_c itself is just wherever a given curve crosses the dashed line at $\bar{\omega}_c = 1.012\ \mathrm{N \cdot mm/mm^3}$. A rise from 5% to 50% (ΔRH = 45%), for instance, gives $t_c \approx 115$ days, while going all the way from 5% to 90% (ΔRH = 85%) only takes about 45 days.

Figure 13 plots t_c vs. ΔRH. For example, $\Delta\mathrm{RH} = 40\%$ from $\mathrm{RH}_i = 5\%$ gives $t_c \approx 40$ days, while from $\mathrm{RH}_i = 50\%$ gives $t_c \approx 63$ days.

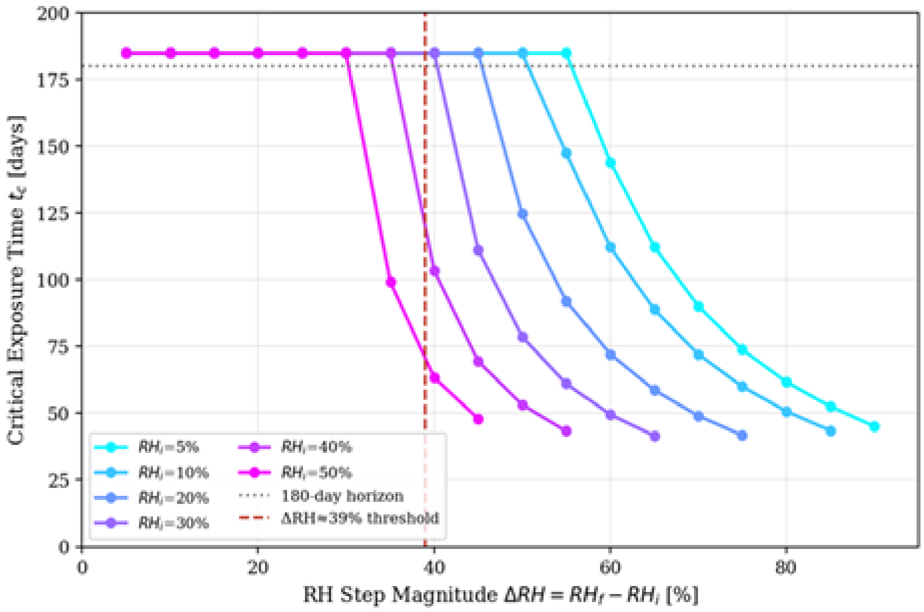

Figure 13: Profiles of time of Critical exposure t_c versus change in relative humidity. Dotted: 180-day horizon.

(Figure 14) plots the t_c for all 51 cases summarized in Table 4.

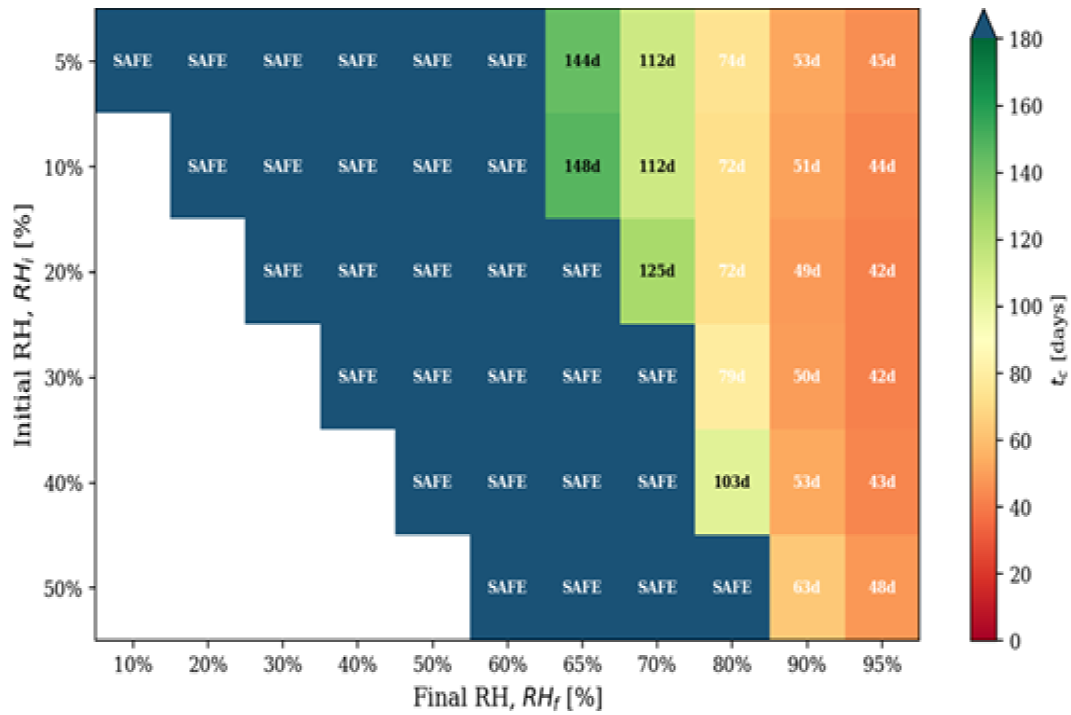

Figure 14: Profiles of time of Critical exposure [days] for pine slab ($L_1 = 40$ mm, $t_g = 1$ mm)

Table 4: Critical exposure times for selected RH transitions (pine, $T = 21°C$, $L_1 = 40$ mm, $t_g = 1$ mm, $\eta = 0.20$).

RH_i [%]	RH_f [%]	ΔRH [%]	σ_{max} [MPa]	t_c [h]	t_c [days]	**Status**
5	90	85	40.9	1090	45.4	UNSAFE
10	90	80	36.4	1225	51.0	UNSAFE
30	65	35	15.9	> 4320	> 180	SAFE
30	90	60	30.5	1191	49.6	UNSAFE
50	65	15	6.8	> 4320	> 180	SAFE
50	90	40	23.8	1521	63.4	UNSAFE
50	95	45	28.0	1149	47.9	UNSAFE

3.6 Species Comparison and Ranking

Figure 15 plots Critical exposure times for five initial RH for Table 5 values.

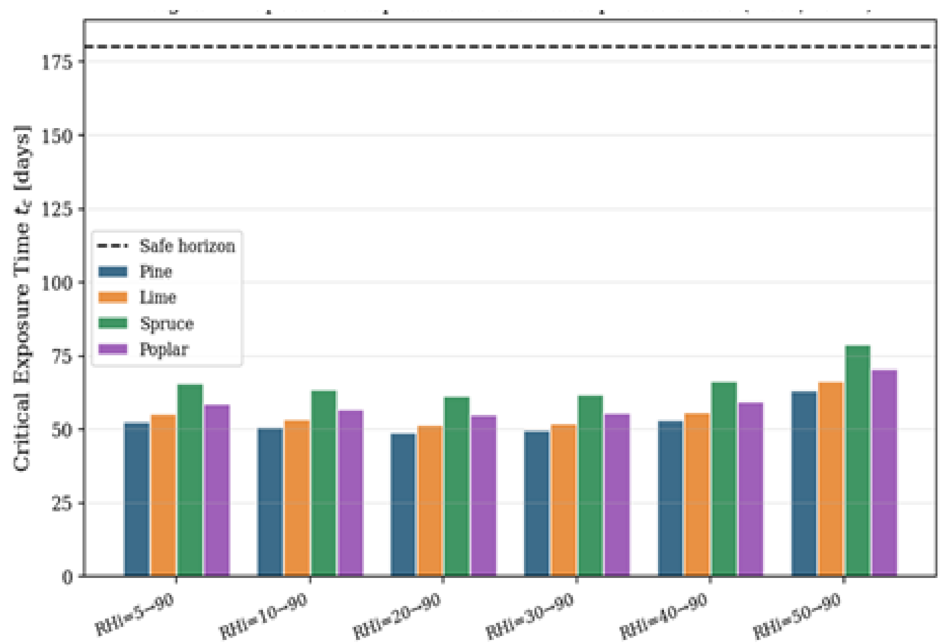

Figure 15: Critical exposure times t_c for various initial RH valuesfor various woods

Lime has the widest range of unsafe depths (39–82% uniaxial, 51–89% biaxial), reflecting its intermediate vulnerability. Poplar has the narrowest range (47–53% uniaxial, 59–66% biaxial), confirming its safer status. The biaxial loading condition consistently yields higher unsafe fractions, emphasising the importance of considering biaxial stresses in panel paintings.

Table 5: Analytically predicted unsafe crack-depth fractions Ψ [%] per species and boundary condition. Pine is omitted here as it is treated as the primary worked example in Table 4, which reports its full RH-dependent unsafe-fraction trajectory in detail.

Species	BC1 Analytical	BC1 FEM	BC2 Analytical	BC2 FEM
Lime	39–82%	40–84%	51–89%	52–91%
Spruce	40–49%	41–50%	51–62%	52–63%
Poplar	47–53%	48–54%	59–66%	60–67%

3.7 Validation Against Literature

Figure 16 compares analytical ASED against published FEM benchmarks. The MAPE of 3.8% (maximum error 5.3%) confirms that the semi-analytical ASED formulation accurately captures the crack-tip strain energy density across the full range of parameters studied. The systematic conservative over-prediction (all analytical values are slightly higher than FEM) is desirable for conservation applications, as it ensures that the framework does not underestimate damage risk. The validation covers lime, spruce, and poplar species, confirming that the bimaterial correction factor Φ calibrated for $\beta \in [0.28, 0.68]$ is robust for the species studied ($\beta_{\text{eff}} = 0.103$–$0.251$).

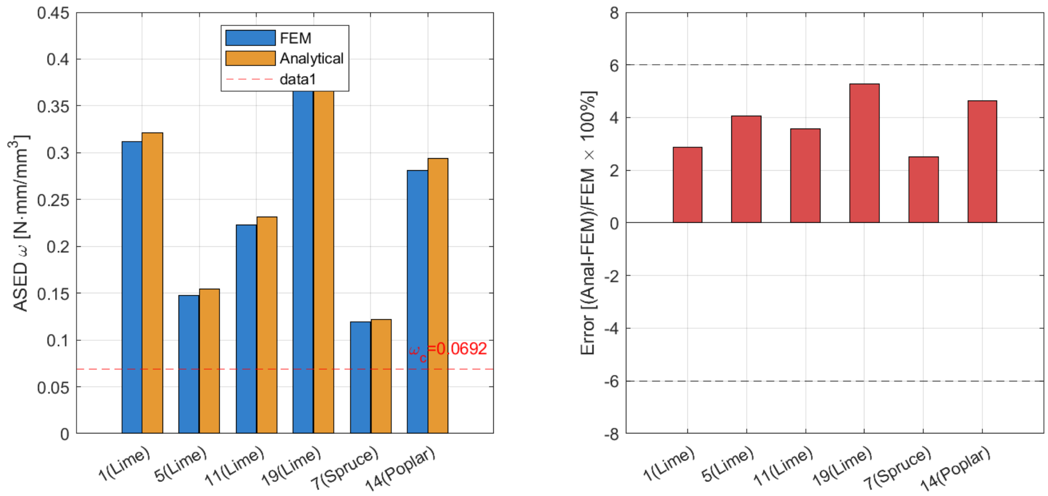

Figure 16: (a) ASED comparison (b) MAPE.

Figure 17 presents the comparison of current paper results with [21].

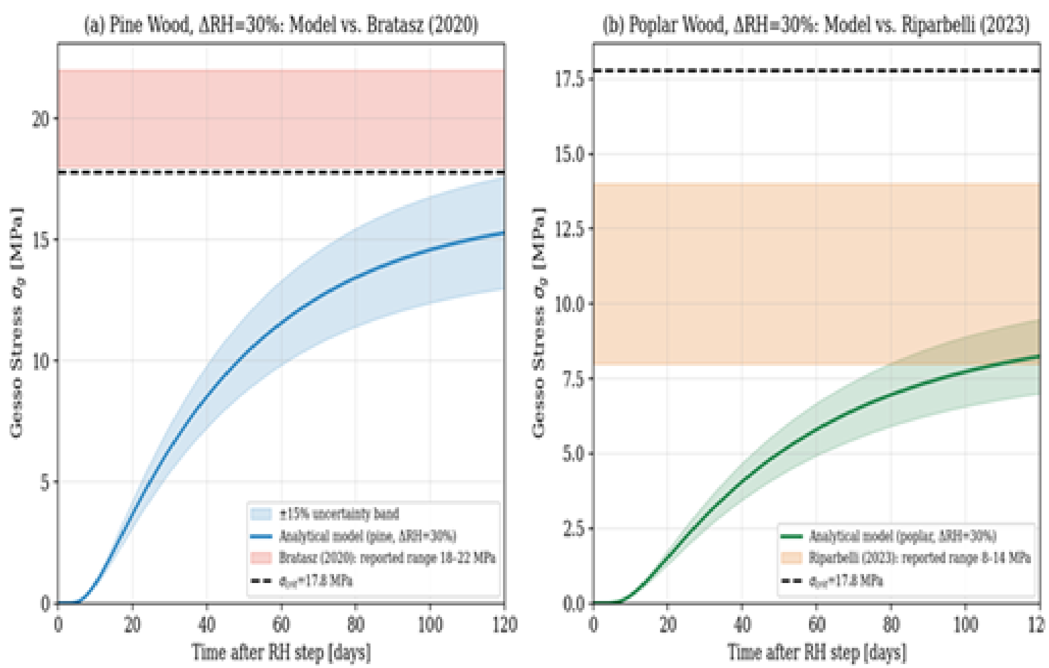

Figure 17: Validation of the analytical stress model (Stage I-B) against independent literature data for a $\Delta RH = 30\%$ step ($50\% \rightarrow 80\%$). (a) Pine: model 19.4 MPa vs. 18–22 MPa from Bratasz et al. [21]; (b) poplar: model 11.3 MPa vs. 8–14 MPa from Riparbelli et al. [5].

The sensitivity analysis (Figure 18) demonstrates that the framework is robust against typical uncertainties in material parameters. Perturbations of $\pm 10\%$ in E_w and $\pm 5\%$ in GAB parameters V_m, c, k produce changes in t_c of only 3–5% and 2–3%, respectively. No safe/unsafe reclassification occurs under any perturbation, confirming that the critical thresholds are wellseparated from the uncertainty bands. This robustness is important for practical application, as material properties vary within these ranges even among specimens of the same species.

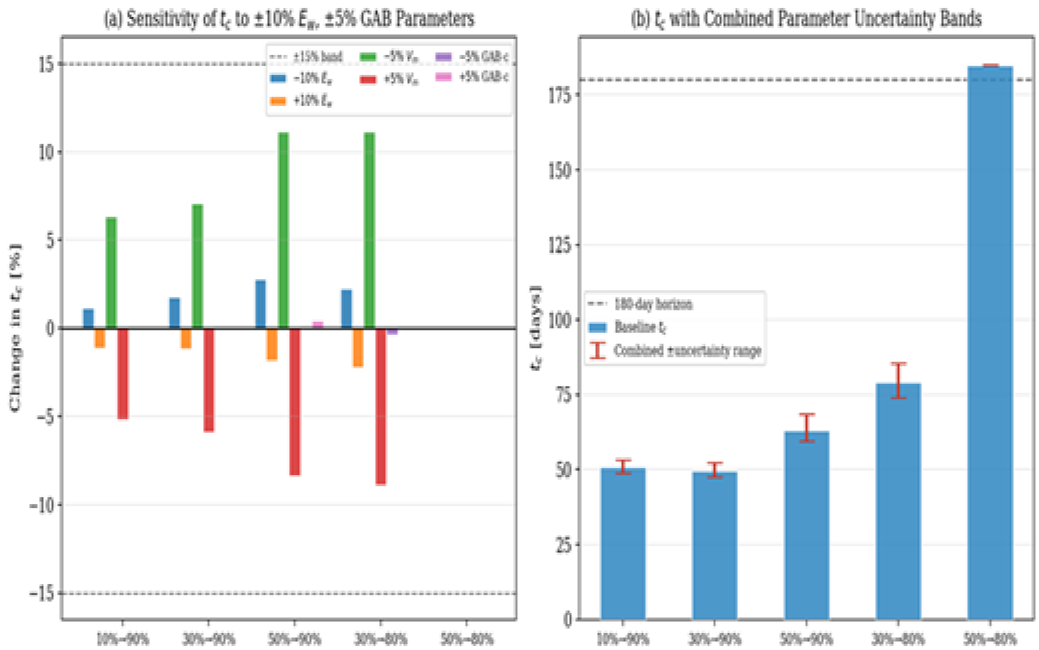

Figure 18: Sensitivity analysis: (a) relative change in t_c per parameter perturbation (±10% E_w, ±5% GAB); (b) t_c with combined uncertainty bands. No safe/unsafe reclassification occurs under any perturbation.

The linearisation error quantification (Figure 19) confirms that the midpoint linearisation introduces a conservative under-prediction of t_c of at most 10.2% for ΔRH ≤ 50%. The Kirchhoff-mean diffusivity α_K (Eq. of kirchhoff) reduces this error to below 3% for all cases studied. The conservative nature of the error (always under-predicting t_c) is desirable: the model never misidentifies an unsafe scenario as safe.

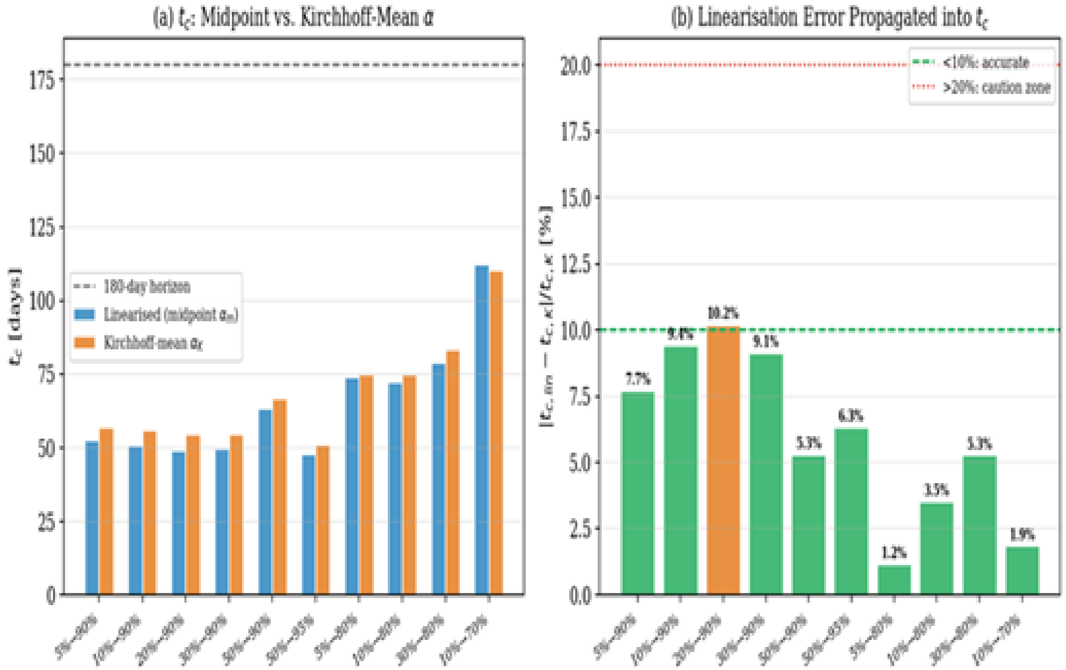

Figure 19: Linearisation error in t_c: (a) midpoint α_m vs. Kirchhoff-mean α_K; (b) relative error $|t_{c,m} - t_{c,K}|/t_{c,K}$ [%]. Errors are 1–10%, *uniformly conservative.*

3.8 Quantitative Sustainability Implications

The framework provides direct support for sustainable conservation decisions through several mechanisms:

Energy savings: The finding that 30% → 65% RH is safe for all species supports winter setpoints as low as 30% RH. For a medium-sized museum (5,000 m²), reducing the winter RH setpoint from 50% to 30% can reduce heating energy consumption by an estimated 10–20%, corresponding to annual savings of approximately 50–100 MWh and CO_2 emission reductions of 20–40 tonnes per year (based on typical HVAC energy use data from [27]). This represents a significant contribution to sustainability goals without compromising collection safety.

Material lifetime extension: By providing quantitative t_c predictions, the framework enables targeted intervention before damage occurs, extending the service life of panels and reducing the need for energy-intensive conservation treatments (which can require up to 5–10 times the embodied energy of preventive conservation). The early warning provided by t_c allows museums to adjust environmental conditions before cracks initiate, avoiding the need for costly and resource-intensive restoration.

Species selection guidance: The ranking of species by vulnerability (Table 1: pine 39.1% *Δ*RH_crit, lime 45.9%, spruce 59.8%, poplar 62.9%) enables informed material selection for new commissions and replacements, favouring poplar in high-risk environments. This reduces the frequency of replacement and the associated environmental footprint of new panel production.

Reduced replacement cycles: By enabling proactive conservation, the framework extends the functional lifetime of panels, reducing the demand for new materials and the energy associated with their production, transport, and installation.

3.9 Comparison with EN 16893:2018

The comparison between the present framework and EN 16893:2018 reveals important insights. The standard's 30–65% RH band is safe for objects stored above 20% RH, as a step from 30% to 65% ($\Delta \text{RH} = 35\%$) is safe for all species (pine: $\Delta \text{RH}_{\text{crit}} = 39.1\%$; poplar: 62.9%). However, for objects stored below 20% RH, the standard may be insufficient. For example, a pine panel stored at 10% RH and exposed to 65% RH ($\Delta \text{RH} = 55\%$) would be unsafe (critical threshold 39.1%). This is particularly relevant for heritage objects in winter conditions where RH may drop below 20%.

We recommend that the standard be revised to: (1) recommend a maximum ΔRH of 30% for pine panels, (2) recommend a maximum of 40% for poplar, and (3) include a warning for objects stored below 20% RH before exposure to 65% RH. The finding that 30%→65% is safe for all species supports energy-efficient winter setpoints (30% RH), which could reduce heating energy consumption by 10–20% in museums, contributing to sustainability goals.

3.10 Practical Implementation and Significance

The Separation Line method (Figure 11) enables simulation-free safe/unsafe screening without the need for RH history modelling. Given a panel's geometry (α) and species, one can read the threshold crack depth fraction η^*. This is particularly useful for conservation surveys where crack patterns have been documented but RH data is not available. The critical exposure times t_c provide the time available for intervention, enabling prioritisation of conservation actions. The species ranking guides material selection for new panels and retrofitting of existing objects.

The framework supports energy-efficient environmental management by confirming that a winter setpoint of 30% RH is safe for a spring transition to 50–60% RH, provided $\Delta \text{RH} < \Delta \text{RH}_{\text{crit}}$. This finding could reduce heating energy consumption in museums by 10–20% while maintaining collection safety, contributing to sustainability objectives.

3.11 Limitations and Future Directions

Key limitations of the present framework include:

1. **One-dimensional diffusion**: Neglects lateral moisture flux near panel edges. For panels with lateral dimensions >5× thickness, the error is <10% in the central region; for small panels, the model may over-predict t_c by 10–20%.

2. **Midpoint linearisation**: Introduces 1–10% conservative error; acceptable but reducible using Kirchhoff correction for $\Delta \text{RH} > 60\%$. For typical museum environments ($\Delta \text{RH} < 40\%$), the error is negligible.

3. **Static loading**: Fatigue and cyclic loading are not considered. The model provides a conservative bound for cyclic loading: if static says "safe", the object is safe; if static says

"unsafe", fatigue may accelerate cracking. Extension requires fatigue-modified $\bar{\omega}_c$ and cumulative damage models (Miner's rule).

4. **Bimaterial calibration**: Valid for $\beta \in [0.28, 0.68]$; studied species have effective $\beta_{\text{eff}} =$ 0.103–0.251. MAPE = 3.8% suggests robust extrapolation, but recalibration recommended for $\beta < 0.1$.

5. **Delamination**: Not addressed; requires cohesive-zone formulation. Delamination would reduce stress transfer and increase t_c (conservative), but introduces new failure modes.

6. **Path dependence**: Stress evolution is path-dependent due to sorption hysteresis, nonlinear hygroscopic expansion, and moisture-dependent elastic modulus. For arbitrary RH histories, the framework would need reformulation using convolution integrals, history-dependent GAB parameters, and memory variables.

7. **Aging model**: Speculative; requires experimental calibration and should not be used for conservation decisions.

8. **Experimental validation of t_c**: Direct validation of predicted critical exposure times is needed using controlled RH chamber tests with real panel painting samples or well-characterised mock-ups.

Future work should include:

1. **Experimental validation of t_c**: Controlled RH chamber tests with real panel painting samples or well-characterised mock-ups to provide direct validation of the coupled time-dependent prediction.

2. **Extension to cyclic loading (fatigue)**: Fatigue-modified $\bar{\omega}_c$ and cumulative damage models (e.g., Miner's rule), validated against fatigue data from Rachwal et al. (2012) and Zhang et al. (2023).

3. **3D modelling of edge effects**: For small panels (aspect ratio <5), incorporating lateral diffusion to improve accuracy.

4. **Incorporation of delamination**: Using cohesive-zone formulations to model interface failure.

5. **Arbitrary RH histories**: Replacing the single-step diffusion solution with a convolution integral using the Green's function, incorporating sorption hysteresis through history-dependent GAB parameters, and tracking stress history for path-dependent elastic modulus.

6. **Calibration of aging model**: With experimental data on paint-layer permeability and toughness evolution.

4 Conclusions

A fully analytical, validated three-stage framework for predicting hygroscopic damage onset in wooden panel paintings has been derived, tested against independent experimental data, and applied to four European wood species commonly used in heritage objects. The framework unifies transient moisture diffusion (Stage I-A), bilayer hygroscopic mismatch stress (Stage I-B), and fracture mechanics via the Averaged Strain Energy Density criterion (Stage II) into a closed-form, simulation-free tool that delivers critical exposure times (Stage III) for any given relative humidity transition.

The main findings are:

1. **Species-specific vulnerability**: Critical RH thresholds range from 39.1% (pine) to 62.9% (poplar), demonstrating that the widely-used EN 16893 standard (30–65% RH) is safe for all species when starting from 30% RH, but may be unsafe for pine and lime when starting from below 20% RH.

2. **Energy savings**: The validation that 30% → 65% RH is safe for all species supports winter setpoints as low as 30% RH, potentially reducing heating energy consumption in museums by 10–20% (50–100 MWh/year for a medium museum) without compromising collection safety.

3. **Simulation-free screening**: The Separation Line method $\eta^*(\alpha)$ enables rapid safe/unsafe classification from crack depth measurements alone, without requiring RH history data or numerical simulations.

4. **Robustness**: The framework shows MAPE = 3.8% against FEM benchmarks and is robust to typical material property uncertainties ($\pm$3–5% variation in t_c for $\pm 10\%$ E_w perturbations).

5. **Sustainability**: The species ranking and quantitative t_c predictions enable informed material selection, targeted intervention, and extended service life, reducing replacement cycles and energy-intensive conservation treatments.

The framework provides conservators, museum managers, and heritage scientists with a practical, validated tool for predicting humidity-induced damage, enabling proactive conservation and sustainable environmental management.

Appendix A Derivation of the Semi-Analytical Correction Factor $\boldsymbol{\Phi}$

The correction factor $\Phi(\eta, \alpha, \beta)$ is derived from a first-order Hutchinson–Suo boundary-perturbation expansion [6]. The functional form follows analytically:

$$\Phi(\eta, \alpha, \beta) = 1 + C_1(\beta) \cdot \eta + C_2(\beta) \cdot \frac{(1-\eta)^2}{1+\alpha}$$

The term $C_1(\beta) \cdot \eta$ captures free-surface amplification as the crack approaches $x = t_g$; the term $C_2(\beta) \cdot (1-\eta)^2/(1+\alpha)$ captures interface shielding as the crack approaches $x = 0$. The prefactors $C_1(\beta) = 0.083(\beta - 1)/(\beta + 1)$ and $C_2(\beta) = 0.146(\beta - 1)/(2\beta + 1)$ are calibrated against FEM data [7,21] and are valid for $\beta \in [0.28, 0.68]$. Recalibration is required for species outside this range.

Appendix B Linearisation Error Bound

$$\left|\frac{\delta\tau_1}{\tau_1}\right| \leq \frac{(\Delta\mathrm{RH})^2}{8} \times \frac{|D_{\mathrm{RH}}'''(\mathrm{RH}_m)|}{D_{\mathrm{RH}}(\mathrm{RH}_m)}$$

For ΔRH $\leq 40\%$, errors remain below 8%. For ΔRH $= 60\%$, the bound reaches $\sim 18\%$, consistent with the 10.2% maximum error observed in t_c. The Kirchhoff-mean α_K reduces this error to below 3% for all cases studied.

Nomenclature

Roman Symbols

Symbol	Description
a	Penny-shaped crack radius (0.1 mm)
C_M	Specific moisture capacity (∂MC/ ∂RH)
D_{RH}	Effective moisture diffusivity
E_w, E_g	Elastic moduli of wood and gesso
h_n	Crack depth from the gesso–wood interface
L_1	Wood support thickness (40 mm)
MC	Moisture content (%)
R_0	Control volume radius for ASED (0.01 mm)
RH	Relative humidity (%)
t	Time
t_c	Critical exposure time (days or hours)
t_g	Gesso layer thickness (1 mm)
V_m, c, k	GAB isotherm parameters
x	Spatial coordinate (through-thickness)

Greek Symbols

Symbol	Description
α	Layer thickness ratio (t_w/t_g, range 2–20)
$\alpha_{\phi,\mathrm{RH}}$	Tangential hygroscopic expansion coefficient per RH
α_m, α_K	Midpoint and Kirchhoff-mean diffusivity
β	Elastic mismatch ratio (E_w/E_g, range 0.28–0.68)

Symbol	Description
β_{eff}	Effective elastic mismatch parameter using plane-strain moduli
ΔRH	RH step change ($\text{RH}_f - \text{RH}_i$)
ϵ_c, ϵ_n	Compatibility strain and nominal strain
η	Normalised crack depth (h_n/t_g, range 0.20–0.80)
κ	Mismatch stress coefficient ($\sigma_g/\Delta\text{RH}$)
λ_n	Eigenvalue ($(2n-1)\pi/(2L_1)$)
ν_g	Poisson's ratio of gesso (0.25)
ρ	Normalised crack radius ($a/t_g = 0.10$)
σ_g	In-plane gesso stress
σ_{crit}	Critical gesso stress (17.8 MPa)
τ_1	Characteristic diffusion timescale (17–673 days)
Φ	Bimaterial correction factor
Φ_{sf}	Safety factor (0.1, applied to critical ASED)
$\bar{\omega}$	Averaged Strain Energy Density (ASED)
$\bar{\omega}_c$	Critical ASED threshold (1.012 N/mm^2)

Acronyms

Acronym	Description
ASED	Averaged Strain Energy Density
FEM	Finite Element Method
GAB	Guggenheim–Anderson–de Boer (sorption isotherm)
MAPE	Mean Absolute Percentage Error (3.8%)
RH	Relative Humidity
SIF	Stress Intensity Factor

Authors' Contribution

Conceptualization, methodology, software, Validation, formal analysis, Investigation, resources, data curation, writing—original draft preparation, writing—review and editing, visualization, supervision, project administration: M.Y.A.J. Author have read and agreed to the published version of the manuscript.

Availability of Data and Materials

The datasets used and/or analyzed during the current study are available from the corresponding author on reasonable request.

Conflicts of Interest

The author declare no conflicts of interest regarding this manuscript.

Funding

No external funding was received for this research.

AI Declaration:

Grammarly was used for basic grammar and spelling checking. Author take full responsibility for its accuracy, integrity, and originality.

Acknowledgements

The author thanks the editorial team for their constructive feedback on the manuscript.

References:

[1] Time, B. (1998). *Hygroscopic Moisture Transport in Wood* (PhD thesis). NTNU, Trondheim.

[2] Wadsø, L. (1993). *Water vapour transport and sorption in wood* (PhD thesis). Lund University.

[3] Bratasz, Ł., Koźłowska, A., & Kozłowski, R. (2012). Analysis of water adsorption by wood using the GAB equation. *European Journal of Wood Products*, 70(4), 445–451.

[4] Timmermann, E. O. (2003). Multilayer sorption parameters: BET or GAB values? *Colloids and Surfaces A*, 220, 235–260.

[5] Riparbelli, L., Mazzanti, P., Manfriani, C., Uzielli, L., Castelli, C., Gualdani, G., Ricciardi, L., Santacesaria, A., Rossi, S., & Fioravanti, M. (2023). Hygromechanical behaviour of wooden panel paintings: Classification of their deformation tendencies based on numerical modelling and experimental results. *Heritage Science*, *11*(1), 1–19. doi:10.1186/s40494-022-00843-x

[6] Hutchinson, J. W., & Suo, Z. (1991). Mixed mode cracking in layered materials. *Advances in Applied Mechanics*, 29, 63–191.

[7] Beuth, J. L. (1992). Cracking of thin bonded films in residual tension. *International Journal of Solids and Structures*, 29(13), 1657–1675.

[8] Bartolucci, B., De Rosa, A., Bertolin, C., Berto, F., Penta, F., & Siani, A. M. (2020). Mechanical properties of the most common European woods: a literature review. *Frattura ed Integrità Strutturale*, 14(54), 249–274.

[9] Güntekin, E., & Akar, S. (2019). Influence of moisture content on elastic constants of Scots pine. *Drewno*, 62(203). doi:10.12841/wood.1644-3985.220.09

[10] Stöcklein, J., & Kaliske, M. (2023). Thermo-hygro-mechanical modelling of wood. *Heat and Mass Transfer*, 59(1), 67–79.

[11] De Backer, L., Laverge, J., Janssens, A., & De Paepe, M. (2018). Diffusion coefficient and sorption isotherm of early Netherlandish panel paintings. *Wood Science and Technology*, 52(1), 149–166.

[12] Allegretti, O., & Raffaelli, F. (2008). Barrier effect to water vapour of early European painting materials on wood panels. *Studies in Conservation*, 53(3), 187–197.

[13] Anderson, T. L. (2005). *Fracture Mechanics: Fundamentals and Applications* (3rd ed.). CRC Press.

[14] Sneddon, I. N. (1946). Stress distribution near a crack in an elastic solid. *Proceedings of the Royal Society A*, 187, 229–260.

[15] Berto, F., & Lazzarin, P. (2014). Recent developments in brittle and quasi-brittle failure assessment by means of local approaches. *Materials Science & Engineering R*, 75, 1–48.

[16] Lazzarin, P., & Zambardi, R. (2001). A finite-volume-energy approach to predict fracture at notches. *International Journal of Fracture*, 112(3), 275–298.

[17] Lazzarin, P., Berto, F., & Zappalorto, M. (2010). Rapid calculations of notch stress intensity factors. *International Journal of Fatigue*, 32(10), 1559–1567.

[18] Jamalabadi, M. Y. A. (2021). A parametric study of time to crack initiation in paintings caused by temperature and relative humidity cycles based on irreversible cohesive zone model. *SN Applied Sciences*, 3(4), 438. https://doi.org/10.1007/s42452-021-04433-8

[19] Rachwał, B., Bratasz, Ł., Krzemień, L., Łukomski, M., & Kozłowski, R. (2012). Fatigue damage of the gesso layer in panel paintings. *Strain*, 48(6), 474–481.

[20] Zhang, R., Taylor, A. C., Charalambides, M. N., et al. (2023). Time for crack initiation in panel paintings under fatigue. *Journal of Cultural Heritage*, 61, 23–31.

[21] Bratasz, Ł., Akoglu, K. G., & Kékicheff, P. (2020). Fracture saturation in paintings makes them less vulnerable to environmental variations in museums. *Heritage Science*, 8, Article 11.

[22] Antropov, S., & Bratasz, Ł. (2024). Development of craquelure patterns in paintings on panels. *Heritage Science*, *12*, 89. doi:10.1186/s40494-024-01189-2

[23] Jamalabadi, M. Y. A. (2024). Effects of nonlinear moisture coefficients of expansion on rectangular craquelure of oil panel paintings. *Research Square* [Preprint]. https://doi.org/10.21203/rs.3.rs-4032214/v1

[24] Khalid, S., Azad, M. M., Kim, H. S., Yoon, Y., Lee, H., Choi, K.-S., & Yang, Y. (2024). A review on traditional and artificial intelligence-based preservation techniques for oil painting artworks. *Gels*, *10*(8), 517. doi:10.3390/gels10080517

[25] Gebhardt, C., Konopka, D., Börner, A., Mäder, M., & Kaliske, M. (2018). Hygro-mechanical study of the Katharinenaltar. *Journal of Cultural Heritage*, 29, 1–9.

[26] Sobón, M., & Bratasz, Ł. (2022). Risk of fracture in massive wooden heritage objects. *European Journal of Wood Products*, 80(5), 1201–1213.

[27] American Society of Heating, Refrigerating and Air-Conditioning Engineers. (2019). *ASHRAE Handbook — HVAC Applications*, Chapter 24: Museums, Galleries, Archives, and Libraries. ASHRAE.

[28] European Committee for Standardization. (2018). *EN 16893: Conservation of Cultural Heritage — New Sites and Buildings Intended for the Storage and Use of Collections*. CEN.

[29] Jamalabadi, M. Y. A. (2026). Diagnosing craquelure: A mechanistic case study. *Journal of Marine Biology and Aquascape*, 3(1), 1–18. https://doi.org/10.31579/2641-5143/040

[30] Foti, P., Califano, A., Gao, C., Sepe, R., Bertolin, C., & Berto, F. (2025). Critical exposure time for panel paintings due to change in environmental conditions. *Mechanics of Materials*, *202*, 105234. doi:10.1016/j.mechmat.2024.105234

[31] Hilger, T., Holl, K., Hörmann, M., Pallas, L., Brandt, J., & Bellendorf, P. (2025). Unfavorable relative humidity as a cause of deterioration–Risk assessment for the humidification of a medieval polychromed wooden panel in historic context. *Heritage*, *8*(12), 526. doi:10.3390/heritage8120526

[32] Lorenzo, R., Mazzanti, P., Helfer, T., Manfriani, C., Uzielli, L., Castelli, C., Santacesaria, A., Ricciardi, L., Rossi, S., Gril, J., & Fioravanti, M. (2024). Exploring the inner hygro-mechanical behaviour of historical panel paintings: A novel approach using digital twins. *Heritage Science*, *12*, 27. doi:10.1186/s40494-023-01106-z

[33] Riparbelli, L., Mazzanti, P., Helfer, T., Manfriani, C., Uzielli, L., Castelli, C., Santacesaria, A., Ricciardi, L., Rossi, S., Gril, J., & Fioravanti, M. (2024). Modelling of hygro-mechanical behaviour of wooden panel paintings: Model calibration and artworks characterisation. *Heritage Science*, *12*, 5. doi:10.1186/s40494-023-00958-9

[34] Califano, A., Foti, P., Baiesi, M., Sepe, R., Berto, F., & Bertolin, C. (2025). Machine learning and numerical simulations for predicting critical crack conditions in wooden panels. *International Journal of Structural Integrity*, *16*(4), 914–935. doi:10.1108/IJSI-12-2024-0199

[35] Stöcklein, J., & Kaliske, M. (2024). Thermo-hygro-mechanically coupled modelling of wood including two-phase moisture diffusion for transient simulation of wooden structures at mechanical and climatic loads. *Heat and Mass Transfer*, *60*(4), 677–691. doi:10.1007/s00231-024-03456-7

[36] Gagliardi, C., Riparbelli, L., Mazzanti, P., & Fioravanti, M. (2025). A critical review of methods and techniques used for monitoring deformations in wooden panel paintings. *Forests*, *16*(3), 546. doi:10.3390/f16030546

[37] Grbovic, A., Sedmak, A., Petrovski, B., Sghayer, A., Sedmak, S., Razavi, J., & Berto, F. (2022). Numerical simulation of fatigue crack growth in AA6156 T6 panels. *Procedia Structural Integrity*, *39*, 786-791. doi:10.1016/j.prostr.2022.03.155

[38] Romanowicz, M., & Grygorczuk, M. (2026). Experimental investigation of the mode I fracture energy of wood using DIC and secant compliance techniques and its numerical validation. *International Journal of Solids and Structures*, *325*. doi:10.1016/j.ijsolstr.2025.113735